

Copyright  
by  
LeuJen Chen  
2015

The Dissertation Committee for LeuJen Chen  
certifies that this is the approved version of the following dissertation:

**Spin-polarized scanning tunneling microscopic study of cobalt cluster  
on HOPG – From instrumentation to real time measurement**

Committee:

---

Alejandro de Lozanne, Supervisor

---

John Markert

---

Maxim Tsoi

---

Zhen Yao

---

Emanuel Tutuc

**Spin-polarized scanning tunneling microscopic study of cobalt cluster  
on HOPG – From instrumentation to real time measurement**

**by**

**LeuJen Chen, B.S.**

**DISSERTATION**

Presented to the Faculty of the Graduate School of  
The University of Texas at Austin  
in Partial Fulfillment  
of the Requirements  
for the Degree of

**DOCTOR OF PHILOSOPHY**

The University of Texas at Austin  
August 2015

Dedicated to my parents and my brother LeuYu.

## **Acknowledgements**

First and foremost, I would like to forward sincere gratitude to my supervisor, Dr. Alex de Lozanne. Unlike most of other research groups, of which the students were trained and gained experimental skills from their senior lab mates, I obtained those abilities directly from Alex. As a professor, Alex still enjoys participating in many hand-on duties in the research. He is the person I worked most often with, and I especially appreciate his kind assistance to my project in many early mornings. He is an expert on designing and building instruments. I learnt a lot of problem solving, logical thinking, and engineering mindset from him. I also watched him coordinating and communicating with many project relevant personnel, and processing things in the most efficient/effective way under limited research budget. Those are all invaluable experiences for people who want to become an experimentalist in the future. I have been playing classical guitar for many years, but has little chance to play in front of audience. Alex happens to be a fan of classical guitar, so we both enjoy a little melody flowing in the air sometimes in our group meeting.

I joined the group at the very beginning of 2010. Ryan was an undergraduate researcher then, and we worked together very often at the time. He taught me quite a lot of machine shop basics, and made a fancy animation of our microscope head loading mechanism. We introduced the core of our STM to the

general audience very easily and clearly through this video. I hope he is doing well in his current career. Seong Heon was the postdoc who joined the lab about the same time as me. Our spin-polarized STM was constructed by him. He passed the whole STM system to me and our most recent SP-STM system is basically the modification of what he left off. There's only a few months' overlap between Frank and I in this lab. He is still coming to lab to hang out with Alex and his previous colleagues in the lab from time to time. Alfred graduated from this lab one year later. He is a confident and talented student who also gave me many sincere advices on finding industrial jobs. We made contact to each other through email several times after his graduation. Neliza was a hard working lab colleague of mine. She always sat at the corner of the lab and building her Hall probe microscope. We have just met each other in this year APS March Meeting. I hope she will find a decent industrial job soon. Morgann is an easy-going person. She likes teaching, so often brought out some interesting general physics puzzle to us. She also taught me to run the commercial AFM in Shih's lab. I appreciate her help. Xin Zhou is the latest graduate of our group. We have the same mother language, so we hang out most often outside of lab. I hope he will doing well in the SPM research after I leave. Francisco, Fernando and Jorge have being undergraduate researchers in our lab for years. Jorge worked with me most often. He made nice tungsten tips for my STM experiment, and the tip quality is improving through time evolution.

I admired all kinds of technical supports that offer to my project on RLM third floor. I have received much assistance from the members of cryogenic-vacuum lab, electronics shop, machine shop, and student shop. Jack

runs the machine shop. He is a case of cold hands, warm heart. He taught and took good care of students who want to make their own hardware. He was always there to talk or help. I've just heard that he was retired recently, it was a pity that I didn't have a chance to say goodbye to him. We have gained immeasurable help from the machine shop. Our STM chamber, main body of STM head and many relevant delicate components were all made by our shop. I met Ed quite often, cause I needed to refill the liquid nitrogen dewar every other day. He is a religious guy and always has a heartwarming conversation with me.

I would also want thank the members of the NSF-MIRT. MIRT members explored interdisciplinary research topics. Being part of it enabled me look at things at a larger scope. Listening to different perspectives from the other departments often shed some light, and also inspired new ideas on my own project.

Among them, Dr. Zhou has long term research collaboration with our group, and kindly provides us bilayer manganite for my STM experiment. I appreciate his sample supply.

Finally I would like to thank my family. Through the skype connection with my mom and dad, my distant friend and family has no less concern of me. My yearning for my beloved motherland was soothed by their laughter and regard. My brother LeuYu is an architect who currently works in Shanghai. I am very proud of him. I could not finish my doctorate degree without their support.

LeuJen Chen June 2015

# **Spin-polarized scanning tunneling microscopic study of cobalt cluster on HOPG – From instrumentation to real time measurement**

Publication No. \_\_\_\_\_

LeuJen Chen, Ph.D.

The University of Texas at Austin, 2015

Supervisor: Alejandro de Lozanne

This dissertation is divided into three parts. The first part provides the introduction and the principles of traditional scanning tunneling microscopy, and then extends the content to the fundamental operation of the spin-polarized variant. The core part describes our home-made sp-STM system in detail, which includes information about the hardware, electronics, and sample/tip preparation. The third part intends to demonstrate the experimental difficulties encountered in doing spin-polarized measurements. We first discuss the elimination of the unpolarized electronic contribution to the overall spectroscopic information on cobalt clusters on graphite (HOPG) system at the nanometer-scale, and then show the possible factors that hinder the atomic-level magnetic study of the spin polarized STM measurement. Preliminary STS analysis of the sample surface is included in the last section.

## Table of Contents

|   |             |
|---|-------------|
| <b>Acknowledgements</b>   | <b>v</b>    |
| <b>Abstract</b>   | <b>ix</b>   |
| <b>List of Figures</b>  | <b>viii</b> |
| <b>Chapter 1. Scanning Tunneling Microscopy</b>                               | <b>1</b>    |
| 1.1 Scanning tunneling microscope .....                                       | 1           |
| 1.2 Principles .....  | 3           |
| 1.3 Operation modes of spin-polarized STM .....                               | 8           |
| <br>  |             |
| <b>Chapter 2. Experimental Setup</b>  | <b>13</b>   |
| 2.1 Scanning tunneling microscope,<br>superconducting magnet and dewars ..... | 13          |
| 2.2 New electronics for piezoelectricpositioners .....                        | 23          |
| 2.3 Tip preparation .....   | 27          |
| 2.3.1 Electrochemical etching .....   | 27          |
| 2.3.2 In-situ tip treatment .....   | 29          |
| 2.3.3 The treatment for spin-polarized STM .....                              | 31          |
| 2.4 Manipulators .....  | 34          |
| 2.5 Vacuum System .....   | 37          |
| 2.6 Vibration isolation .....   | 39          |

|   |           |
|---|-----------|
| <b>Chapter 3. Scanner tube calibration</b>  | <b>44</b> |
| 3.1 STM scanner tube calibration . . . . .  | 44        |
| <b>Chapter 4. STM of Cobalt clusters on HOPG</b>  | <b>48</b> |
| 4.1 Motivation . . . . .  | 48        |
| 4.2 The model of graphene and graphite. . . . .   | 49        |
| 4.3 Electronic contribution elimination to the overall<br>spectroscopy . . . . .          | 53        |
| 4.4 Identification of cobalt clusters behavior on HOPG . . . . .                          | 54        |
| 4.5 Preliminary spectroscopic study of cobalt cluster<br>and impurities on HOPG . . . . . | 62        |
| 4.6 Conclusions . . . . .   | 67        |
| 4.7 Suggestion for future works . . . . .   | 67        |
| <b>Appendix</b>   | <b>69</b> |
| <b>Bibliography</b>   | <b>70</b> |
| <b>Vita</b>   | <b>75</b> |

## List of Figures

|       |  |    |
|-------|--|----|
| 1.1   | The nutshell of STM. . . . .   | 3  |
| 2.1.1 | Top, bottom and side views of the Pan type walker legs . . . .   | 15 |
| 2.1.2 | 3D model of the STM body. . . . .  | 16 |
| 2.1.3 | Photograph of RT/LT STM body. . . . .  | 17 |
| 2.1.4 | Photographs and schematic of superconducting magnet and its<br>removable current carrying leads. . . . . | 19 |
| 2.1.5 | Schematic of the STM vacuum chamber. . . . .   | 20 |
| 2.1.6 | Schematic of STM dewar. . . . .  | 22 |
| 2.2.1 | Schematic of Slip-stick motion. . . . .  | 23 |
| 2.2.2 | Diagram of the conventional sawtooth voltage input that<br>generates Pan- type walking. . . . .          | 24 |
| 2.2.3 | Schematic of the simplified electronics that drives a Pan- type<br>motor. . . . .                        | 25 |
| 2.2.4 | Waveforms of two consecutive piezoelectric plates shown in<br>different color traces. . . . .            | 26 |
| 2.3.1 | Schematic view of static electrochemical etching of tungsten<br>wires. . . . .                           | 28 |
| 2.3.2 | Photograph of conical-shaped electrochemical etched tungsten<br>tip. Magnification: 400x. . . . .        | 29 |
| 2.3.3 | Schematic of electron bombardment setup. . . . .   | 30 |
| 2.3.4 | Photograph of coating tungsten tip with cobalt. . . . .  | 32 |

|       |   |    |
|-------|---|----|
| 2.3.5 | STM image of Co cluster deposited on HOPG at 80 kelvin. .   | 33 |
| 2.4.1 | (a) Schematic of a typical magnetically-coupled feedthrough with translational and rotational motions. (b) The component of (1) in (a) of our load-lock manipulator. (c) Photograph of the load-lock manipulator. (d) Photograph of the vertical manipulator. . . . | 35 |
| 2.4.2 | (a) Schematic of the sample/tip grabber. It is the component 6 in figure 2.4.1(a) of our main manipulator. (b) Photograph of component 1 and 2 in figure 2.4.1(a) of our main manipulator   | 37 |
| 2.5.  | Schematic of STM vacuum system. . . . .   | 38 |
| 2.6.1 | Diagram of upper support for the vacuum chamber. . . . .  | 40 |
| 2.6.2 | Photograph of the whole STM system. . . . .   | 41 |
| 2.6.3 | Photograph of the top of STM body. . . . .  | 42 |
| 3.1.1 | Large field of view of RT STM topographic images. (a) Image of $x=0.32$ LSMO. (b) Image of gold on mica. . . . .  | 45 |
| 3.1.2 | (a) Uncalibrated 80K STM image of HOPG. (b) Contour line along the green dotted line in (a). . . . .  | 46 |
| 3.1.3 | (a) Calibrated 80K STM image of HOPG. (b) Contour line along the green dotted line in (a). . . . .  | 47 |
| 4.2.1 | Atomic structure of graphene. . . . .   | 50 |
| 4.2.2 | The first Brillion zone of graphene reciprocal lattice. . . . .   | 50 |
| 4.2.3 | Simplified $\pi$ bands of graphene. . . . .   | 51 |
| 4.3   | (a) STM image of Co cluster on HOPG at 80K. Size of the image is 100x100 nm. (b) I-V spectroscopic curves taken at the selected locations in (a). . . . .   | 54 |

|       |   |    |
|-------|---|----|
| 4.4.1 | STM topographic images taken on (a)5/9/2015 (b)6/23/2015.   | 55 |
| 4.4.2 | (a) STM topographic image of Co clusters on HOPG (b) dI/dV map of (a).  | 56 |
| 4.4.3 | Consecutive STM topographic images with totally 6.5 hours acquisition time. (n)is the conductance map of (m).   | 58 |
| 4.4.4 | Contours along lines (A), (B), (C) in figure 4.3.3 (m).   | 59 |
| 4.4.5 | 2D FFT of figure 4.3.3.   | 60 |
| 4.4.6 | Consecutive STM images. Image (b) has combined simultaneous dI/dV curves at the blue spots. The topographic distortion phenomenon at the blue spots is persistent over a wide setpoint current range. | 62 |
| 4.5.1 | STM topography and simultaneous 64x64 grid dI/dV spectroscopy of Cobalt cluster on HOPG.  | 63 |
| 4.5.2 | dI/dV curves acquired above the cobalt clusters on graphite.  | 63 |
| 4.5.3 | dI/dV curves acquired above (a,b) bare HOPG, (c) 2nm away from Co cluster and (d) localized topographic defect. Right figure set is the blow up around Fermi level of the left set.                   | 64 |

## Chapter 1

### Scanning Tunneling Microscopy

#### 1.1 Scanning tunneling microscope

The scanning tunneling microscope (STM) was invented by Binnig and Rohrer in 1981. This is an instrument designed for imaging surface structure which is based on the concept of quantum tunneling. STM is eligible to explore materials whose resistivity is lower than  $1\Omega\cdot\text{cm}$ . The essential elements of STM are six parts: sensor, scanner, coarse-approach stepper, controller (includes scanning and feedback electronics), computer and vibration isolation (The nutshell of STM is shown in figure 1.1).

STM tips are usually made from W(tungsten) metal or Pt-Ir (platinum-iridium) alloy. The very end atom of the tip contributes 90% of the tunneling current, whereas including the second layer of the pyramid atoms combined contribute almost 99% of the current. The current decays exponentially with the tunneling gap, therefore changing distance by only 1 angstrom can change the current ten-fold. Upon applying a voltage to the z-piezo, the tip and the sample are brought to within a fraction of a nanometer each other. By applying a bias voltage between the tip and the sample, a tunneling current is generated. The tunneling current is converted into a voltage and then amplified. The result is

compared with a reference value, and the difference is used to drive the z piezo. Once tunneling is established, the relative distance between tip and sample is varied and the changes of current are mapped as images. There are two major operating scan modes of the STM: constant current mode uses feedback to keep the tunneling current constant by adjusting the height of the scanner at each measurement point. The second mode of operation is the constant height mode where the tip scans along a plane parallel to the average topography of the surface, and the variation of the current due to the local changes in tip-sample distance is recorded.

In addition to basic surface topography, information of electronic structure at a given location in the sample can be acquired simultaneously. According to Bardeen theory, the current to voltage derivative is  $dI/dV$  proportional to energy density of states. By sweeping voltage and measuring  $dI/dV$  at a specific location, a plot of the local density of states (LDOS) as a function of energy is obtained. This type of measurement is called scanning tunneling spectroscopy (STS).

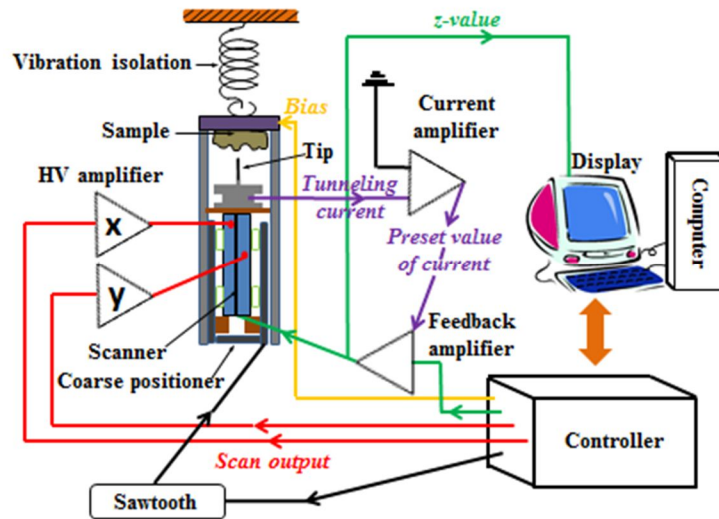


Figure 1.1 The nutshell of STM.

## 1.2 Principles

The most widely applied theory for the tunneling phenomenon in solids as well as in STM is Bardeen's first-order perturbation theory (one dimensional single-electron version). Although the inclusion of further correction factor transfers the theory into three-dimensional version, is more pertinent to the physics of STM, the original Bardeen theory is fair enough to explain the general picture of how the STM works.

The wave functions of electrode A and B (usually refer to as sample and tip) satisfy the Schrodinger equation:

$$i\hbar \frac{\partial \Psi}{\partial t} = \left[ -\frac{\hbar^2}{2m} \frac{\partial^2}{\partial z^2} + U_{A,B} \right] \Psi \quad (1.2.1)$$

where  $U_{A,B}$  is the potential function of electrode A or B. The stationary states are

$$\Psi = \psi_\mu e^{-iE_\mu t/\hbar} \quad ; \quad \Psi = \chi_\nu e^{-iE_\nu t/\hbar} \quad (1.2.2)$$

with the spatial wave functions and energy eigenvalues satisfying:

$$\begin{aligned} \left[ -\frac{\hbar^2}{2m} \frac{\partial^2}{\partial z^2} + U_A \right] \psi_\mu &= E_\mu \psi_\mu; \\ \left[ -\frac{\hbar^2}{2m} \frac{\partial^2}{\partial z^2} + U_B \right] \chi_\nu &= E_\nu \chi_\nu \end{aligned} \quad (1.2.3)$$

By defining a tunneling matrix element as:

$$M_{\mu\nu} = \int_{z>z_0} \psi_\mu U_B \chi_\nu^* d^3\mathbf{r} \quad (1.2.4)$$

an explicit expression of tunneling current can be derived. If the density of states of both electrodes does not vary appreciably near the Fermi level on the applied bias voltage  $V$ , the tunneling current is

$$I = \frac{2\pi e^2}{\hbar} |M_{\mu\nu}|^2 \rho_B(E_F) \rho_A(E_F) V \quad (1.2.5)$$

The tunneling current  $I$  is proportional to bias voltage  $V$ . It can be conveniently written in terms of tunneling conductance  $G = I/V$  as:

$$G = 2\pi^2 G_0 |M_{\mu\nu}|^2 \rho_B(E_F) \rho_A(E_F) \quad (1.2.6)$$

Using Eq. 1.2.3, the integral in Eq. 1.2.4 can be converted into a surface integral only depending on the unperturbed wave functions of the two electrodes at the separation surface. The integration over  $z$  can be carried out to obtain

$$M_{\mu\nu} = \frac{\hbar^2}{2m} \int_{z=z_0} \left[ \psi_\mu \frac{\partial \chi_\nu^*}{\partial z} - \chi_\nu^* \frac{\partial \psi_\mu}{\partial z} \right] dx dy \quad (1.2.7)$$

Bardeen's theory provided a sound basis for the interpretation of the observed tunneling spectroscopy. Using Eq. 1.2.5, the tunneling current at a bias voltage  $V$  can be evaluated by summing over all relevant states. With a bias voltage  $V$ , the total tunneling current is

$$I = \frac{4\pi e}{\hbar} \int_{-\infty}^{\infty} [f(E_F - eV + \epsilon) - f(E_F + \epsilon)] \times \rho_A(E_F - eV + \epsilon) \rho_B(E_F + \epsilon) |M|^2 d\epsilon \quad (1.2.8)$$

where  $f(E) = (1 + \exp[(E - E_F)/k_B T])^{-1}$  is the Fermi distribution function. The quantities  $\rho_A(E)$  and  $\rho_B(E)$  are the density of states (DOS) of electrode A and B respectively.

If, in the energy range of interest, the following conditions hold: (1) the tip state is spherically symmetric; (2) the tunneling matrix element does not depend on energy level; (3) the tip DOS is a constant over the energy interval of interest; and (4) the sample DOS varies in energy not much in each  $kT$ ; the

Tersoff-Hamann model can be used to simplify Bardeen's expression of tunneling current, Eq.1.2.8 as:

$$\begin{aligned}
 I &= \frac{4\pi e}{\hbar} \int_0^{eV} \rho_T(E_F - eV + \epsilon) \rho_S(E_F + \epsilon) |M|^2 d\epsilon \\
 &\approx \frac{4\pi e}{\hbar} \rho_T |M|^2 \int_0^{eV} \rho_S(E_F + \epsilon) d\epsilon
 \end{aligned} \tag{1.2.9}$$

Using the Tersoff-Hamann expression of tunneling matrix element,  $M \propto \psi(\mathbf{r}_0)$ , where  $\mathbf{r}_0$  is the center of curvature of the tip, the tunneling current is proportional to

$$I \propto \int_0^{eV} \rho_S(E_F + \epsilon, \mathbf{r}_0) d\epsilon \tag{1.2.10}$$

The *dynamic tunneling conductance* at bias voltage  $V$  can be obtained by differentiating Eq. 1.2.10.

$$G(V) \equiv \left( \frac{dI}{dU} \right)_{U=V} \propto \rho_S(E_F + eV, \mathbf{r}_0) \tag{1.2.11}$$

The above quantity can be easily computed using first-principles numerical methods, and it represents an elementary simple model for scanning tunneling spectroscopy.

In spin-polarized STM, the tunneling conductance depends on the relative orientation of the magnetization density vector of tip and sample, which originates from an unequal density of state distribution at the Fermi level with respect to spin. Similar to Eq.1.2.6, the total tunneling conductance is

$$G = 2\pi^2 G_0 |M_0|^2 (\rho_{A\uparrow}\rho_{B\uparrow}|M_{\uparrow\uparrow}|^2 + \rho_{A\uparrow}\rho_{B\downarrow}|M_{\uparrow\downarrow}|^2 + \rho_{A\downarrow}\rho_{B\uparrow}|M_{\downarrow\uparrow}|^2 + \rho_{A\downarrow}\rho_{B\downarrow}|M_{\downarrow\downarrow}|^2) \quad (1.2.12)$$

Where

$$M_0 = \frac{\hbar^2}{2m} \int_{\Sigma} [\psi \nabla \chi^* - \chi^* \nabla \psi] \cdot dS \quad (1.2.13)$$

and,

$$\begin{pmatrix} M_{\uparrow\uparrow} & M_{\uparrow\downarrow} \\ M_{\downarrow\uparrow} & M_{\downarrow\downarrow} \end{pmatrix} = M_0 \begin{pmatrix} e^{i(\phi+\psi)/2} \cos(\theta/2) & \frac{ie^{i(\phi-\psi)/2} \sin(\theta/2)}{e^{-i(\phi+\psi)/2} \cos(\theta/2)} \\ ie^{i(-\phi+\psi)/2} \sin(\theta/2) & e^{-i(\phi+\psi)/2} \cos(\theta/2) \end{pmatrix} \quad (1.2.14)$$

$\psi$ ,  $\theta$  and  $\phi$  are three Euler angles. Eq. 1.2.12 can be expressed in a more concise form by introducing the spin-average density of states

$$\rho_A = \rho_{A\uparrow} + \rho_{A\downarrow} \quad , \quad \rho_B = \rho_{B\uparrow} + \rho_{B\downarrow} \quad (1.2.15)$$

the spin-polarized density of states

$$m_A = \rho_{A\uparrow} - \rho_{A\downarrow} \quad , \quad m_B = \rho_{B\uparrow} - \rho_{B\downarrow} \quad (1.2.16)$$

and also two dimensionless spin polarization parameters,  $P_A$  and  $P_B$ , defined as

$$P_A \equiv \frac{m_A}{\rho_A} \quad , \quad P_B \equiv \frac{m_B}{\rho_B} \quad (1.2.17)$$

,then the tunneling conductance is:

$$G = 2\pi^2 G_0 |M_0|^2 \rho_A \rho_B (1 + P_A P_B \cos\theta) \quad (1.2.18)$$

For processing experimental data, Eq. 1.2.18 is often expressed as

$$G = G_{sa} + G_{sp} \cos\theta \quad (1.2.19)$$

where  $G_{sa}$  is the spin-averaged tunneling conductance, and  $G_{sp}$  is the spin-polarized tunneling conductance [1].

### 1.3 Operation modes of spin-polarized STM

The Tersoff-Hamann model interprets STM images well up to the nanometer scale. But if we want to reach atomic resolution, it is necessary to consider the convolution of both tip and sample electronic states. The simplification of s-wave tip is no longer valid. For example, the STM tips are usually made of either transition metals, for example, Ir, Pt, and W, or semiconductor, Si. The d(notably  $d_z^2$ ) or p(notably  $sp^3$ ) states can dominate the tip DOS. An extension of the Tersoff-Hamann theory toward consideration of tip states with orbital quantum number  $l \neq 0$  was introduced by Chen [2]. Based on more generalized expression, when considering magnetic materials of tip and sample, an additional spin dependence of the tunneling current was derived by Wortmann [3] as:

$$I(\vec{r}_0, V, \theta) = I_0(\vec{r}_0, V) + I_{sp}(\vec{r}_0, V, \theta) = \frac{4\pi^3 c^2 \hbar^3 e}{k^2 m^2} [\mathbf{n}_t \widetilde{\mathbf{n}}_s(\vec{r}_0, V) + \overline{\mathbf{m}}_t \widetilde{\overline{\mathbf{m}}}_s(\vec{r}_0, V)] \quad (1.3.1)$$

The current was measured at the tip position  $\vec{r}_0$  and with an applied bias voltage  $V$ .  $\mathbf{n}_t$  is the non-spin-polarized LDOS at the tip apex,  $\widetilde{\mathbf{n}}_s$  is the “energy integrated” LDOS of the sample.  $\overline{\mathbf{m}}_t$  and  $\widetilde{\overline{\mathbf{m}}}_s$  are the corresponding vectors of the (energy integrated) magnetic LDOS, with

$$\widetilde{\overline{\mathbf{m}}}_s(\vec{r}_0, V) = \int_0^{eV} \overline{\mathbf{m}}_s(\vec{r}_0, \epsilon) d\epsilon \quad (1.3.2)$$

There are three major types of mode for sp-STM. They are (A) Constant-current mode, (B) Spin-resolved spectroscopic mode, and (C) Modulated tip magnetization mode. The content of mode(C) will be skipped here, since the manufacture of the tip is more demanding and time consuming. Also, its highly sensitive characteristic of both in and out-of-plane magnetization direction was later found to be easily achieved by the other modes.

#### (A) Constant current mode

The principles of constant current mode for sp-STM and conventional STM are the same. From eq.(1.3.1), we know that the current includes both spin-average and spin-polarized contributions. However, to study the magnetic properties of the sample, we don't need extra effort to extract spin-polarized component from overall tunneling current by using constant current mode. This

is because the unit cell of magnetic superstructures is always larger than a non-magnetic primitive unit cell. So if expressing tunneling current in a 2D Fourier expansion with respect to the reciprocal surface lattice vector, we can see that the STM images are primarily dominated by the “smallest” nonvanishing reciprocal lattice vector.

The constant current mode has ultimate resolution in magnetic imaging. However, this kind of mode has two limitations: (1) It cannot be adopted in the case of rough surfaces, since the larger scale of the topographic features will interfere with the magnetic structure information. (2) According to eq.(1.3.2),  $I_{sp}$  is only sensitive to the energy integrated spin polarized LDOS. The  $I_{sp}$  signal could be reduced if the spin polarizations of the contributing electronic states change sign in the energy range between the Fermi level and  $eV$ . Therefore, for magnetic structure studies, the constant current mode is only suited under the condition of small applied bias voltage.

#### (B) Spin-resolved spectroscopic mode

In Analogy to conventional STS, spin-resolved spectroscopy also studies the  $dI/dV$  signal by adding a small ac-bias voltage (well above the cutoff frequency of the feedback loop) to a dc-bias voltage. The resulting current modulation is amplified by means of the lock-in technique. Take derivative of e.q.(1.3.1), we have:

$$\frac{dI}{dV}(\mathbf{R}_t, V) \propto \mathbf{n}_t \mathbf{n}_s(\mathbf{R}_t, E_F + eV) + \overline{\mathbf{m}_t \cdot \mathbf{m}_s}(\mathbf{R}_t, E_F + eV) \quad (1.3.3)$$

From the above equation, we know that the conductance contains the information of both spin-average and spin-polarized part. SP-STTS is a powerful tool to study fine magnetic structure of the sample, yet interpreting the measured signal is sometimes complicated and challenging. If we are looking at an electronically homogeneous sample, the interpretation is relatively straightforward, since the spatial variation of the image only comes from the second term of e.q.(1.3.3). Usually, we take large field topographic image first, and then focus the dI/dV map at some desired area with a random bias voltage setpoint. Normally we can identify some kind of “domain” boundary from the observed pattern at this point. We then take the tunneling spectra above adjacent domains. (If we want to acquire a sharper dI/dV map, we conduct the measurement again using bias setpoints that correspond to the local maximums of the tunneling spectra signal. They can be either filled or empty surface states). Based on these spectra, the spin asymmetry can be defined as [4]:

$$A(V) \equiv \frac{\frac{dI}{dV_{\uparrow}(V)} - \frac{dI}{dV_{\downarrow}(V)}}{\frac{dI}{dV_{\uparrow}(V)} + \frac{dI}{dV_{\downarrow}(V)}} \quad (1.3.4)$$

, and the spin polarization of the sample is given by:

$$P_s(V) = \frac{A(V)}{P_t \cos\theta} \quad (1.3.5)$$

where  $P_t$  is the spin polarization of the tip, and  $\theta$  is the angle between tip and sample magnetization directions.  $P_t$  is usually treated as constant for a given

range of applied bias voltages, and the value can be adopted from published data. This simplified approach is found to match nicely with other spin-polarized techniques.

For samples which possess inhomogeneous electronic states, we follow the same analytical path until we get an asymmetric  $A(V)$ . We then compare the two  $dI/dV$  images obtained at the bias voltage of maximum (magnetic contrast image) and zero (electronic contrast image) asymmetry. The magnetic and electronic information of differential tunneling conductance can then be separated.

## Chapter 2

### Experimental Setup

#### 2.1 Scanning tunneling microscope, superconducting magnet and dewars

The desired configuration of our spin polarized STM is able to maintain high rigidity and minimum heat capacity. So the dimension of the body needs to be small and compact. The designs are inspired by the work of Pan [6] [7], but we modify the feet of the coarse approach motor as simple piezoelectric plates [8] rather than shear piezoelectric stacks. These plates are long and thin (25x5x0.3mm PZT5H), offset by 60° with respect to one another (figure 2.1.2(a)). The plate can withdraw and advance a rectangular piece of sapphire plate, which one side of the plate is glued to the walker leg (see figure 2.1.1). One side of the sapphire surface touches against the boron nitride pads on the central stainless steel. A self lubricating boron nitride pad sliding on a hard sapphire surface makes a perfect condition for stick-slip motion. If one use the same dimensions and materials, our closed structure of STM head is more rigid compared to the open structure of Pan's original design, which enables us to use a smaller diameter cylinder.

The support structure for the scanner tube consists of four T-shaped legs and two I-shaped legs. One set (two T-shaped legs and one I-shaped leg) is located at the top, and the other set is at the bottom. The T legs are fixed to the

body with screws, and the I legs are pressed by a leaf spring: a rectangular piece of beryllium copper sheet. We have manually adjusted the tightness of the springs, and found the optimal radial pressure. At room temperature, the result can let approach motor operated up as low as 45V, down as 35V. Due to the temperature dependence of piezoelectric constants, operation at low temperatures requires higher voltage. At 80K, the threshold driving voltage is about 120V in both directions. We put white epoxy to secure the spring tightness after finding its optimal setting, and let white epoxy be cured in at room temperature air.

All electrical contacts to the STM are detachable. The beauty of it is that we can fix the broken wires fairly easy without detaching the helium dewar and the chamber (there is very little chance that the inner contacts may break), and also makes overall construction configuration rigid and compact. The connections are made with 24 gold-plated, cup-shaped contacts that are pointing upward from an insulating ring of the inner connector stage. The STM body has 24 matching phosphor bronze wires that touch against the gold cups. The electrical contacts are made by the weight of STM head itself. The weight of the STM body (including an attached cooper heat sink plate) is about 417g. (see figure 2.1.3)

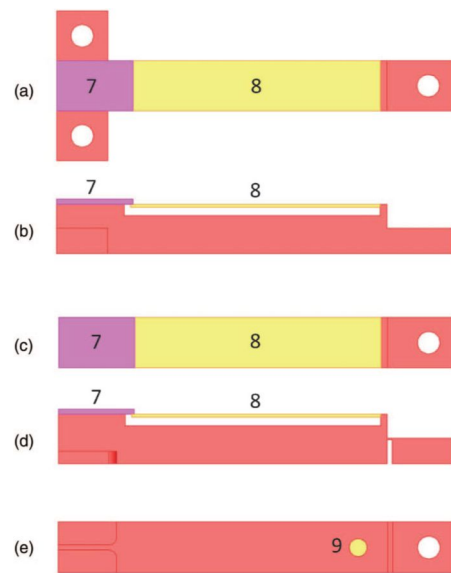


Figure 2.1.1 [9] Top, bottom and side views of the Pan type walker legs. (a) and (b) belong to T-shaped leg, whereas (c),(d) and (e) are I-shaped legs. (7) is the sapphire plate, which has one end glued to piezoelectric plate(8). The top side of piezo plate electrode is shorted to the body (pink part). (9) is the clearance hole for a phosphor bronze wire that makes electrical contact to the bottom electrode of the plate.

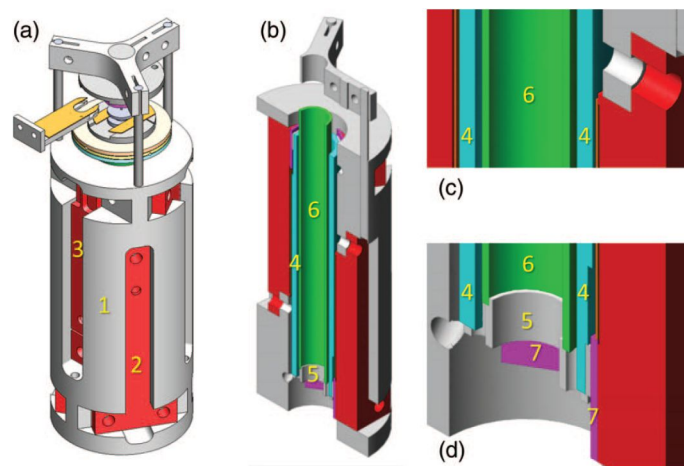


Figure 2.1.2 [9] 3D model of the STM body. (a) (1) is the stainless steel body, (2) is one of the four T-shaped legs and (3) is one of the two I-shaped legs. In(b) (c) (d), (6) is the quadrant electrode piezoelectric scan head, which the bottom part was glued to the MACOR base(5) and therefore bonded to the outer stainless steel pipe(4) [10]. (7) is the sapphire plate of the walker leg which rubs against the boron nitride pad (not labeled) to make smooth slip-stick motion.



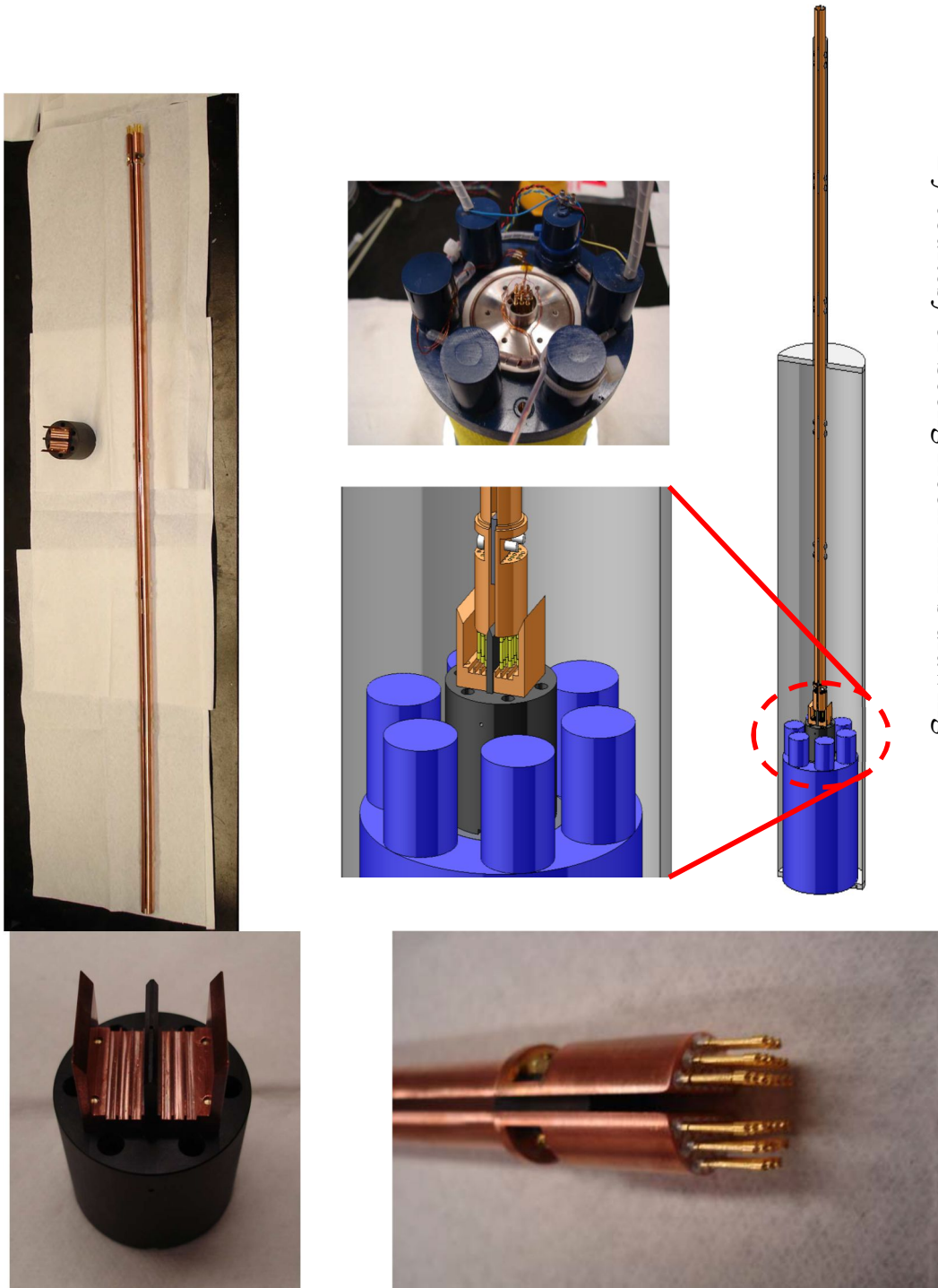
Figure 2.1.3 Photograph of RT/LT STM body. A quarter coins on the left gives a comparison to the exact dimension of the body.

The superconducting magnet we use can provide magnetic field up to 8 T, with dimension of outer diameter of 4.3 inches, height of 6 inches, and with an inner diameter of 2 inches. The weight is 9.6 lb and achieves 8 T with 78 A of current. Due to the uprising cost of liquid helium, we try to reduce coolant consumption when operating the high current magnet. To fulfill this goal, we minimize the heat load by making current-carrying leads removable. Pogo pins on the magnet are used as spring-loaded action for temporary electrical contact, pressed by a current carrying lead (see figure 2.1.4).

The current carrying leads were made by a long copper tube that was split in the middle and re-joined with six insulating supports. We estimate heat

dissipation of each side of the lead be 6W when operating magnet at maximum current 78A. This will boil liquid helium in about 8.4l./hr rate. This rate is much higher than what we observed. The possible explanation is that the exiting cold air of helium/nitrogen gas will cool down the lead along the thin neck of the dewar, thus lowering the consumption rate. Note that our helium dewar has a capacity of only 6 liters.

The STM chamber can be mainly described by two parts (figure 2.1.5). One extends vertically, which houses the stainless steel dewars. The second part is relatively short in length and extends horizontally. This is the main space where we transport or prepare tip/sample, and the front part of it is connected to the ion pump. The vertical section of the chamber has a flexible heating strip wrapped around it in a spiral pattern and is covered with fiberglass insulation and aluminum sheet. This allows an uniform temperature rise while baking and also cool the chamber down to 4°C due to the absorption of radiation by the liquid nitrogen dewar.



By courtesy of Seong Heon Kim's drawing

Figure 2.1.4 Photographs and schematic of superconducting magnet and its removable current carrying leads.

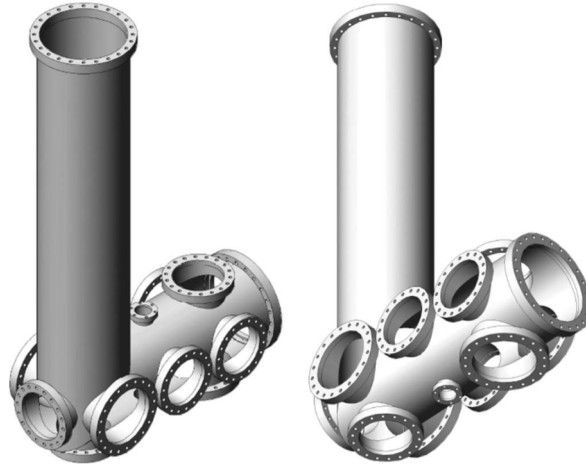


Figure 2.1.5 [9] Schematic of the STM vacuum chamber.

The helium dewar has a capacity of 6 liters while the nitrogen dewar has a capacity of 15 liters. To maintain stabilized LT-UHV environment around 77K, we normally fill the inner dewar with LN2 once a week and fill the outer dewar every day. The bottom of the helium dewar houses a cavity which was made from a copper pipe (figure 2.1.6). This is a space that provides a UHV, low temperature environment for the STM. The superconducting magnet is mounted coaxially right outside of the copper cavity. The neck of the dewar is welded to a soft bellow that is in turn welded onto a 6.75- inch conflat flange. This flange has six 1.33- inch flanges for electrical feedthroughs. Currently, only three out of six are used, the others are saved for future use. The first feedthrough is the electrical contacts for high voltage components (piezoelectric plates and x/y electrodes).

The second flange houses the pin connectors for electrical feedback loop and also the thermal diode contacts. Additional BNC connector on the flange provides the junction of z electrode and GND.

To prevent collapse from atmospheric pressure, five aluminum rings are used to reinforce the structure at the inner wall of the liquid nitrogen dewar.

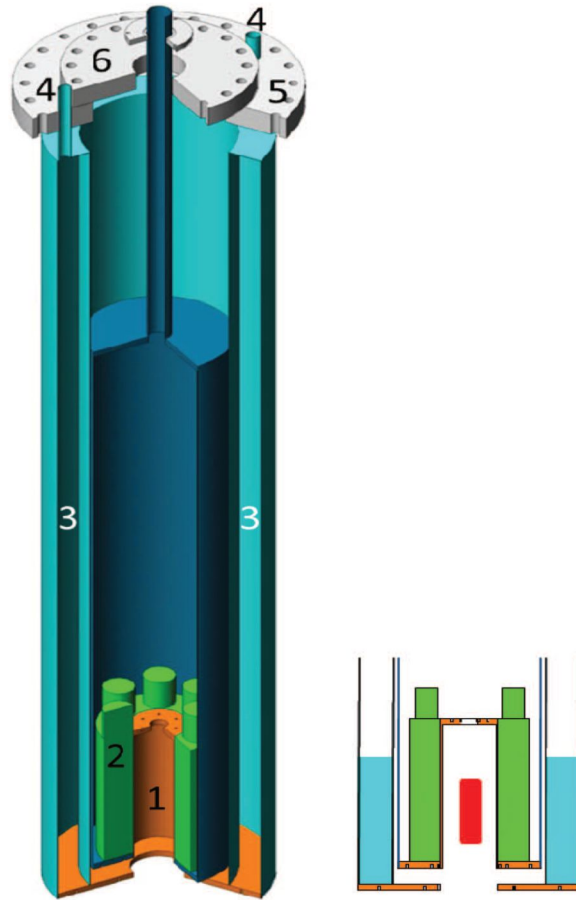


Figure 2.1.6 [9] Schematic of STM dewar. A 6.75 in. flange (6) mates with the adapter 10 in. flange (5) and is welded to the other end of the soft bellows. (1) is the garage for STM body, surrounded by superconducting magnet (2). The superconducting magnet is immersed in the liquid helium environment. The navy blue part of the diagram (not labeled) is the inner dewar that contains LHe. Liquid nitrogen dewar(3) is coaxially outside of inner the inner dewar. We can fill LN2 into the dewar through one of the two openings (4). Two dewars do not touch each other.

## 2.2 New electronics for piezoelectric positioners

The driving mechanism principle of our coarse positioner is the slip- stick motion [11] [12]. According to inverse piezoelectric effect, an electric potential difference can generate a dimension change in piezoelectric materials. By this

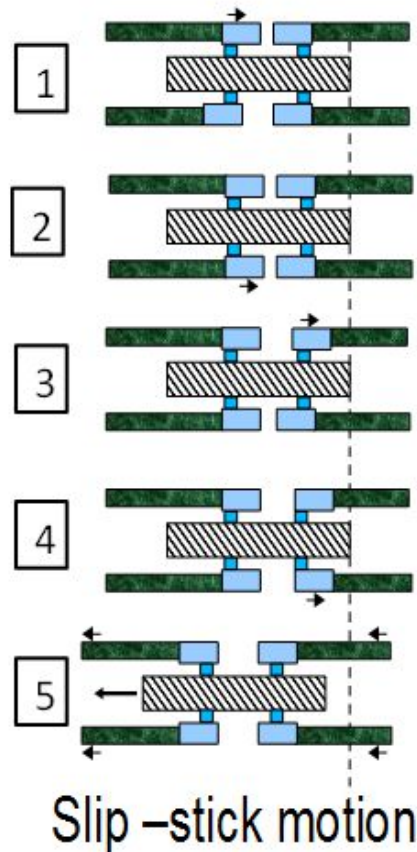


Figure 2.2.1 Schematic of Slip-stick motion. In procedure 1 to 4, applying a sharp voltage step to the piezo plates will make them extend or contract consecutively. Changing an individual dimension at a time will not will not move the central shaft since it cannot overcome the threshold friction between the other plates to the shaft. This is the “slip” part of the motion. In procedure 5, gradual reverse voltage applied to all piezo plates at the same time. The piezo plates change their dimensions simultaneously, so they in turn move the central shaft. This is the “stick” part of the motion.

simple logic, if we design and input a sequential voltage waveform to the body, the relative contacting force of the materials due to dimensional change of the piezo plate will eventually move the scanner at the center, as shown in Figure 2.2.1.

Conventionally, the voltage pattern of an approach motor has a sawtooth shape (see figure 2.2.2). The electrical circuit to generate this kind of pattern is fairly complicated. Instead, we use a very cheap and relatively simple electronics that can perform an equivalent function. The main character of this design is (1) replace the traditional linear ramp with an exponential rise or decay of charge or discharge behavior of a simple RC circuit (C indicates the piezoelectric plates in the STM), (2) use an electromechanical double pole double throw relay switch to generate a fast change in voltage and (3) use one of the two poles in the relays to generate a cascading sequence of switching events. The main part of the circuit is shown in Fig. 2.2.2. We have tested this electronics performance by using a computer to trigger the relay cascade, which we have done by using pin 2 (or any pin 2-9) in the printer port under BASIC programming [13].

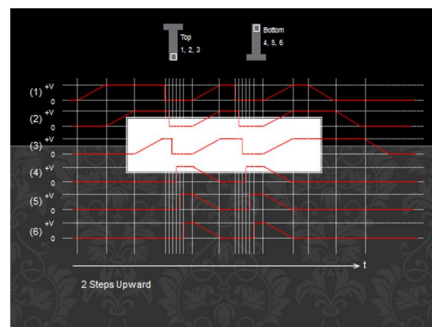


Figure 2.2.2 Diagram of the conventional sawtooth voltage input that generates Pan-type walking.

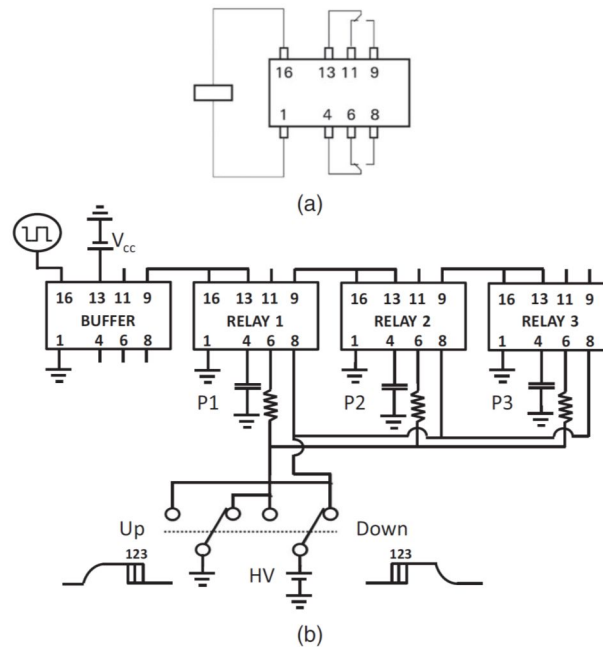


Figure 2.2.3 [14] (a) A double throw, double pole relay. The input coil is between pin 1 and 16. When the coil is unpowered, pin 4 and pin 13 are closed to pin 11 and pin 6 respectively, and is opened to pin 9 and pin 8 respectively. When the coil is powered, the configuration of the loops is the other way around. (b) Schematic of the simplified electronics that drives a Pan-type motor (in reality, we use six relays instead.) A buffer relay is needed since most oscillators do not have enough current to power all relays in the sequence. Additionally, some kind of relays can manually switch the direction of motion as shown at the bottom of the diagram.

Figure 2.2.4 shows the waveform that generated by our electronics. In our case  $C = 20 \text{ nF}$  and  $R = 0.98 \text{ M}\Omega$ , so the decay time constant is  $\sim 20 \text{ ms}$ .

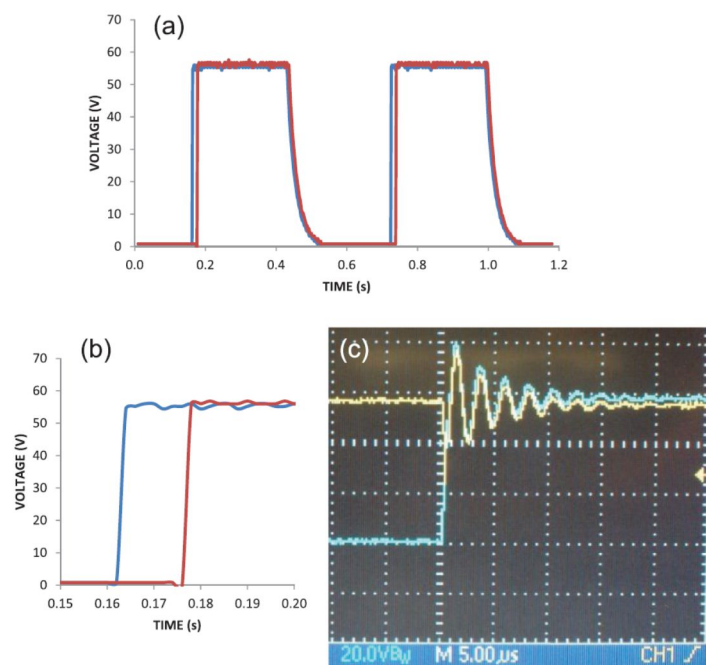
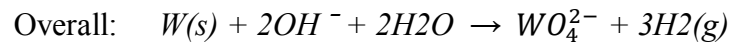
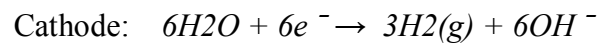
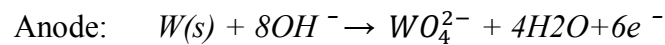


Figure 2.2.4 Waveforms of two consecutive piezoelectric plates shown in different color traces. (a) Two periods of waveforms. (b) blow up of the voltage increase part in (a), note that there is a 8ms delay between the two waveforms. (c) The waveform measured by the oscilloscope. The ringing observed in (c) is too fast for the piezoelectric transducers to follow, so it is of no concern.

## 2.3 Tip preparation

### 2.3.1 Electrochemical etching

STM tips are prepared from low cost 10mil diameter polycrystalline tungsten wires by electrochemical etching. The wire needs to be cleaned with fine sand paper first before etching. A 2M NaOH solution is used as the electrolyte. During etching the current through the membrane will decrease linearly with time because the resistance of the cell increases when the area of the wire in the electrolyte decreases. We track the current values and keep them more or less the same. During the etching process, the following reactions take place [15]:



The wire eventually breaks. The dropped part falls into a container and will be collected as our etched tip. The final apex shape depends on the meniscus thickness and current value, could be an exponential or a conical shape probe. Figure 2.3.2 shows a photo of one of our conical shape tips viewed under the optical microscope.

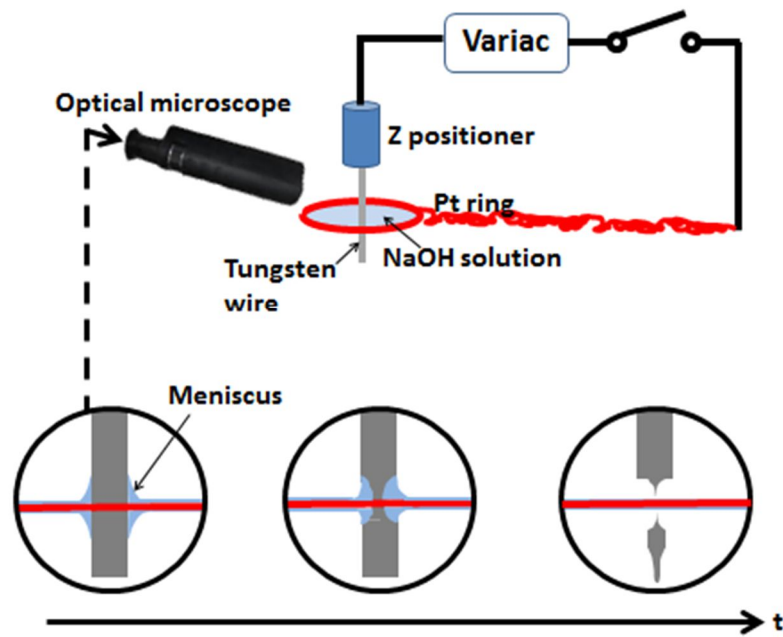


Figure 2.3.1 Schematic view of static electrochemical etching of tungsten wires.

Prior to UHV sharpening, the etched tips were cleaned in distilled water and isopropyl alcohol by ultrasonic rinsing for 5 minutes long respectively.

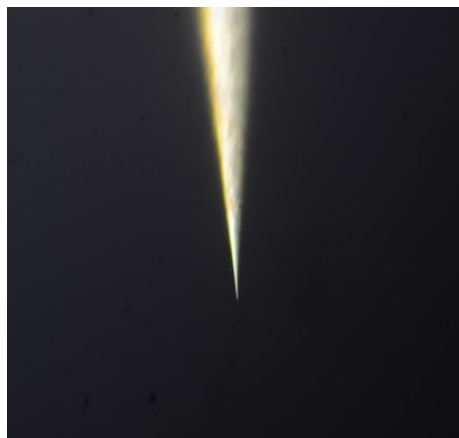
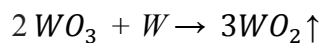


Figure 2.3.2 Photograph of conical-shaped electrochemical etched tungsten tip.  
Magnification: 400x.

### 2.3.2 In situ tip treatments

To reach atomically resolved imaging, the tip's contamination (oxide) needs to be removed, so a second stage cleaning process is necessary. Consecutive electron bombardment in situ is used to fabricate fine, clean W tips. We use the filament of a 13.3 Watt, 12.8 Volt, 1.04 Amp S-8 Miniature Bulb as the hot source of field-emitted electrons. The  $WO_3$  on the tip will then react with W according to:



We heat the tip at the temperature above  $\text{WO}_2$  sublimation temperature ( $800^\circ\text{C}$ ), but well below W melting point. Two steps are involved in in-situ treatment. The first step is stationary heating, which fulfills the task of reorienting the atoms near the tip apex into a more taper-like, sharp overall configuration. We normally heat the tip for 5 minutes at 5W (1000V high voltage and 5mA emission current). The second step is flash heating, which is responsible for removing oxide contamination. We heat the tip at 20W for 20 cycles. To keep track of the flashing time in an easier manner, we make each cycle last for 30 seconds, with 3 seconds power-on and 27 seconds power-off. By utilizing our homemade main manipulator, we can easily place the tip near the evaporation source in vacuum (Figure 2.3.3).

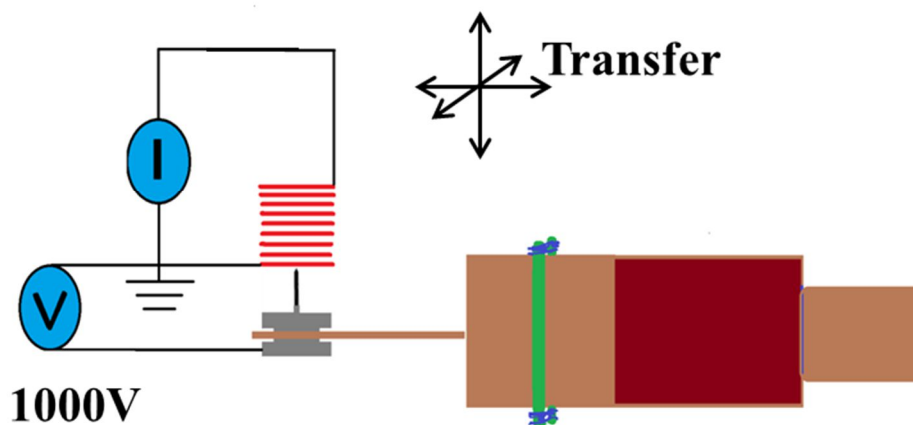


Figure 2.3.3 Schematic of electron bombardment setup.

### 2.3.3 Tip (& sample) treatment for spin-polarized STM

The operation of SP-STM requires that both tip and sample are spin-polarized. However, as mentioned in Section 1.3, a rigorous magnetic structure analysis of the sample needs comparisons of data acquired from magnetic and non-magnetic tips. Before depositing Co on HOPG, the sample needs to have radiation heating for 90 minutes, in order to create clean substrate. Figure 2.3.4 shows a topographic image of Co clusters deposited on HOPG. This image was acquired with a non-magnetic W tip. The Co clusters (bright spots) can be clearly identified. The tip apex was placed about 3.5 cm below the Co source during deposition, with 3.9W coating power for 30 seconds.

The base pressure of our STM system is  $< 1 \times 10^{-9}$  torr, and the pressure inside the cryogenic garage will be at least one order of magnitude lower than that. Under this circumstance, the buildup rate of adsorbed adatoms on the sample surface should be very low. This was proved by running STM images over a few weeks. The change of density of the bright spots is negligible, so we can claim that the sample is stable for prolonged time if it was prepared properly. The magnetic tip, however, sometimes needs to be re-prepared. Even using identical tunneling parameters, the good scanning conditions can go away next time if we don't conduct consecutive data acquisition. The source of the problem is hard to identify. It could either be the tip is away from the previous scanning section due to thermal drift (the preferable area is sometimes very localized), or the configuration of the tip was changed. If we cannot find a good scanning area within few microns away from the previous location, we will re-prepare the tip. The good scanning condition is usually reproducible after re-preparing the tips.

The method of preparing magnetic tip is, (1) go through the procedure as in section 2.3.2, this will move old Co materials away and re-sharpen the apex if we are preparing a previously used tip. (2) place the tip about 5cm below the evaporating source (Figure 2.3.5) and deposit Co on the tip at 5W evaporating rate for 40 minutes. Right after deposition, the tip is annealed at a higher temperature (by increasing power supply's output to the filaments) for 4 minutes and the magnetic tip is transported to the cryogenic garage as fast as possible.

Both for preparing tip and sample, the magnetic material source needs to be degassed at 3.9W for 20 minutes, in order to remove any contamination on the Co source surface.

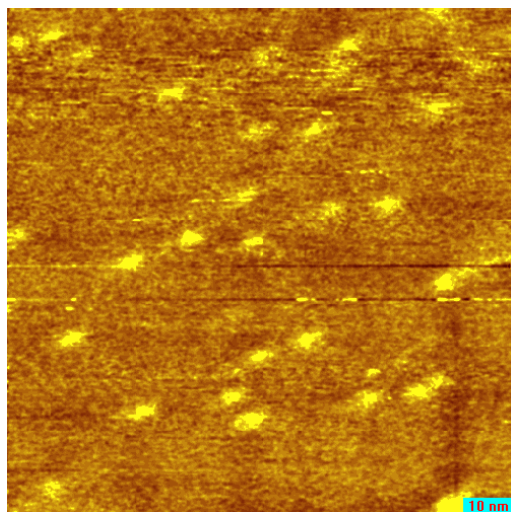


Figure 2.3.4 STM image at 80K of Co clusters deposited on HOPG at room temperature. The size of image is 100x100 nm. The tunneling parameters are: setpoint bias  $V = +1V$ , and a setpoint current  $I = 500pA$ . The resolution is 512x512 pixels, with scan speed of 100nm/s.



Figure 2.3.5 Photograph of the coating procedure on a tungsten tip with cobalt. The tip apex is located about 5cm underneath the Co source bulb. The Co source is heated by three neighboring, equilateral oriented filaments.

For the time being, the two magnetic material sources in our evaporator are all cobalt wires. We might change at least one of them into antiferromagnetic material (chromium for example) in the future, if at the time we want to obtain atomic-level magnetic structure. This can make stray magnetic field from the tip be negligible.

## 2.4 Manipulators

Our STM system has three manipulators: Load lock manipulator, vertical manipulator, and main manipulator. The magnetically coupled characteristics make themselves capable of grabbing small tip/sample holder or STM body in an ultrahigh vacuum environment. They provide both linear and rotary motion inside chamber.

The designs of load lock and vertical manipulator are relatively simple. We can have a general idea of how magnetic-coupled feedthrough work from Figure 2.4.1(a) [16]. A carriage with magnets (1) in vacuum system responds to the movement of an external magnet ring (2) due to ferromagnetic interaction. The head of a long pipe (3) is connected to the carriage, while the other end of it is connected to a grabber (6) that used to transport sample and tip. The pipe (3) is supported and aligned with the outer pipe by a bushing (4) that is fixed with respect to the outside flange (5). High-strength NdFeB permanent magnets with thick nickel coating are used as our source of ferromagnetic interaction materials. The magnets are arranged in a circle with their magnetization axes pointing radially and with alternating polarities between neighboring magnets. Our previous design used aligned ball bearings to let the carriage roll along the length of the pipe and a separate set of ball bearings to allow rotational motion. Our current design replaces ball bearings with four graphite pads (Figure 2.4.1(b)) because we found that if the long pipe is not absolutely straight and round, the movement is a little bit rough, and the self lubricating graphite pads can decrease moving friction significantly, hence reduce the risk of decoupling the inner and outer magne

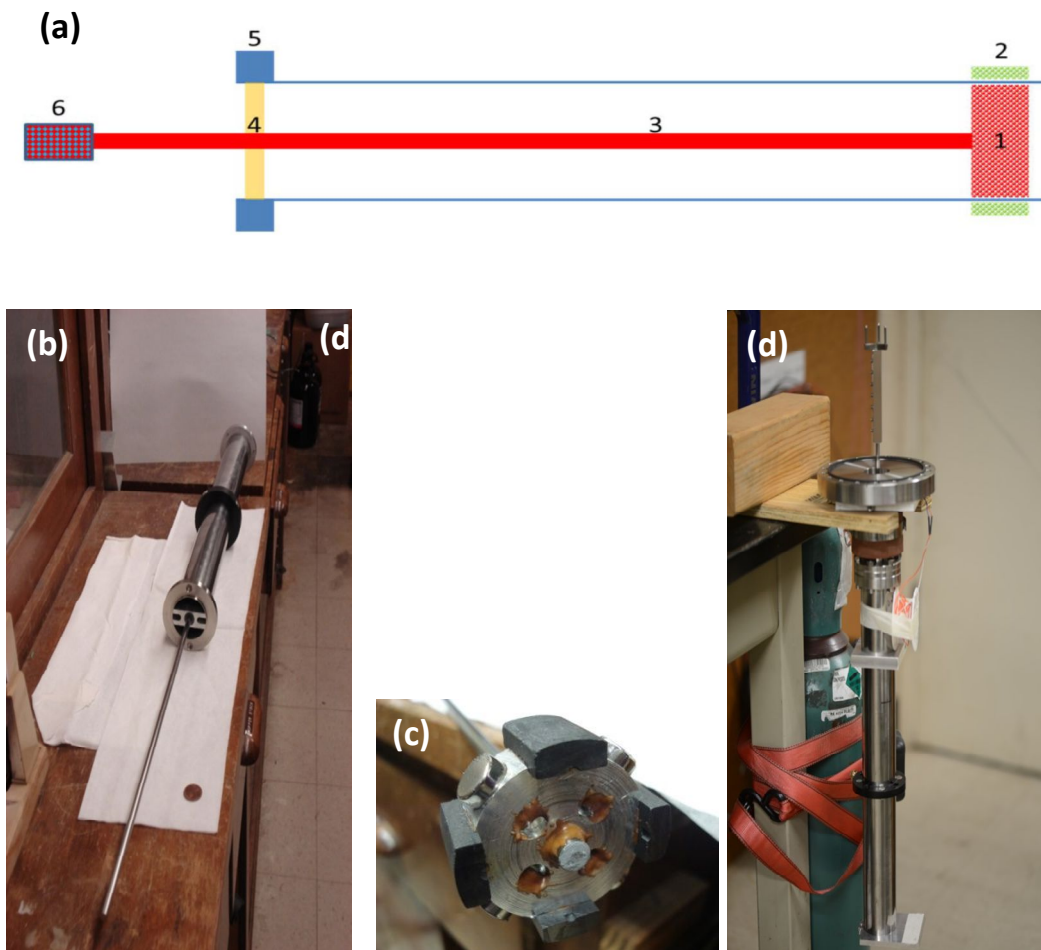


Figure 2.4.1 (a) [18] Schematic of a typical magnetically-coupled feedthrough, with translational and rotational motions. (b) The component of (1) in (a) of our load-lock manipulator. (c) Photograph of the load-lock manipulator. (d) Photograph of the vertical manipulator. The tripod on the top is designed to hold the STM securely when loading and withdrawing STM in from the cold coaxial garage. The mirror right under the tripod is used to reflect laser beam, which can finely control the STM rotary position in vacuum.

The main manipulator has the same type of magnetic-coupled feedthrough as the other two manipulators, but has one additional degree of freedom to open and close a sample/tip grabber (Figure 2.4.2(a)). It is activated by the relative rotation of the first and second set of magnets. A half inch pipe fits in the opening (O) of the grabber head (H). Inside this pipe lies a coaxial quarter inch rod which has 1/4-28 male thread on one end. The male thread matches the female counterpart at (T). While rotating both the magnetic rings on the main manipulator simultaneously makes the grabber rotate, rotating solely the second set of magnets (Figure 2.4.2(b)) makes the 1/4-28 male thread advance, therefore pushing the ceramic piston (P) and in turn pushes the jaws (E) open. Two ceramic rods (green circles in the schematic) serve as pivot points and electrical isolation. A thin teflon sheet is inserted between J and H to also isolate electrical conduction. The red arrow in the photographic inset of figure 2.4.2(a) shows the extension springs that constrain the jaws. The jaws then serve like a fine tweezers to grab a tip/sample holder with a 1/8 inch diameter neck.

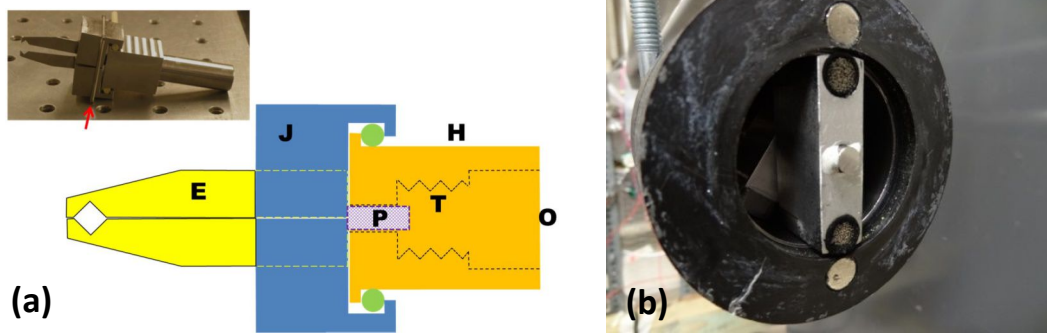


Figure 2.4.2 (a) [18] Schematic of the sample/tip grabber. It is the component 6 in figure 2.4.1(a) of our main manipulator. (b) Photograph of component 1 and 2 in figure 2.4.1(a) of our main manipulator.

The grabber is isolated from ground for voltages up to a few thousand volts. By applying a positive high-voltage to the grabber, we are able to heat a tip or sample holder near the hot filament, which makes heating by electron bombardment fairly easy to carry out.

## 2.5 Vacuum System

The vacuum system of our STM mainly consists of two parts. The first one is the main chamber, attached with an 8 inches flange to a Varian Starcell ion pump with a pumping speed of 230 L/sec. The e-beam evaporator stage is located inside the main chamber. The second part of the system is the load-lock chamber, connected with a cart that has turbo and a rotary pump. It can keep the

chamber vacuum base pressure when we change the tips/samples. Additional titanium sublimation pump is used to further reduce the pressure. With the help of our homemade manipulators and monitoring cameras from different window flanges, we are able to change and prepare tip/sample within about 30 minutes.

Figure 2.5 is the cartoon of the main chamber. Note that vertical manipulator is located right beneath the STM garage. The ion pump is at the bottom of the main chamber and the TSP, aligned with the ion pump, is attached with a 6.75 inches flange to the top of the main chamber. They are blocked by the main chamber through the perspective of view in Figure 2.5.

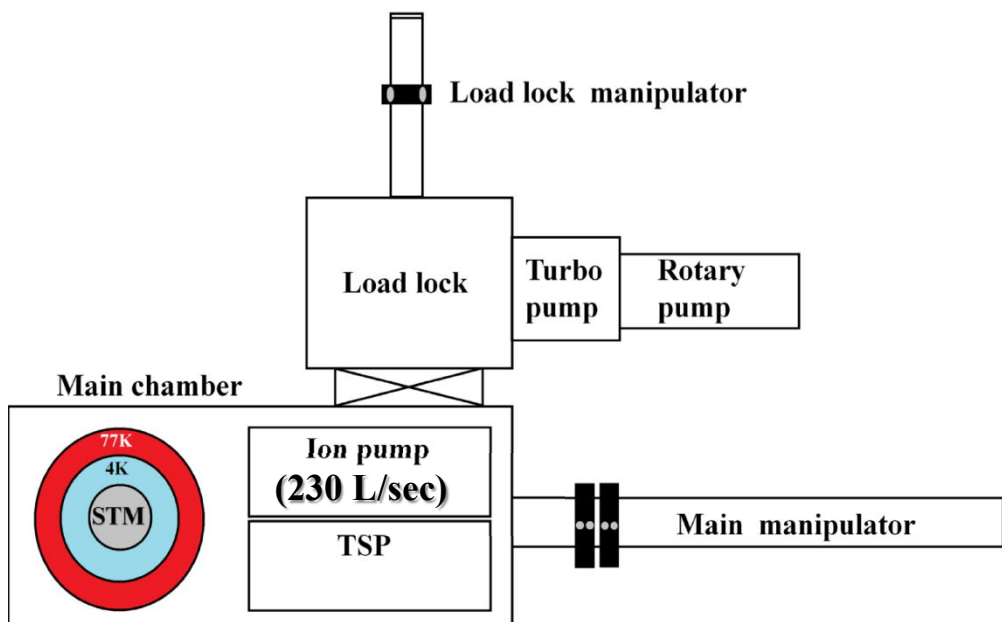


Figure 2.5 Schematic of STM vacuum system (top view).

## 2.6 Vibration isolation

Our STM chamber is supported by only two points. On top of the nitrogen dewar, a bolt of the 10-inch conflate flange is replaced with a threaded rod as shown in Figure 2.6.1. The other end of the threaded rod passes through a clearance hole of a supporting aluminum rod which lies across the wood beams. The second supporting point is at the other end of the chamber. We use a stainless steel cable to hang the front of main chamber through an anchor point on the supporting wood frame. Three pink granite columns, which weigh about 1000 lb each, 12 by 12 by 72 inches, construct the base of the outer supporting system (See Figure 2.6.2). The three columns are locked together with a few pairs of parallel wood beams. At the center of the bottom of each column lie pneumatic pads [17], so the whole system is lifted like a three-legged stool. We adopted wood beams rather than metal a frame as the vibrational isolation material is because of its low cost. Also, its low Q characteristic enables it to damp nearly all frequency vibrational noise more efficiently than metal.

The functions of the 24 phosphor bronze leads on the STM head (see figure 2.6.3) are not only the electrical junction between STM and controller, but their flexible characteristics also may provide the spring force for suppressing the vibration noise. Good electrical contacts are fulfilled by the weight of STM body itself.

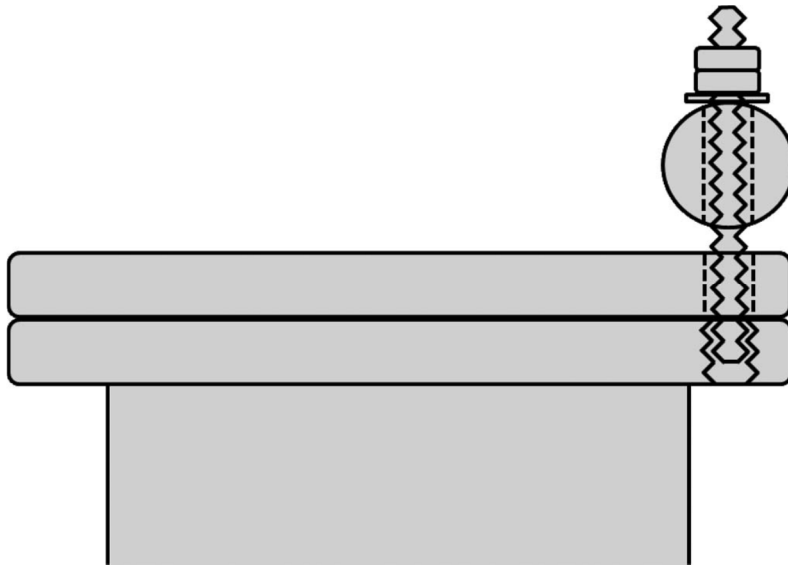


Figure 2.6.1 [9] Diagram of upper support for the vacuum chamber.



Figure 2.6.2 Photograph of the whole STM system.

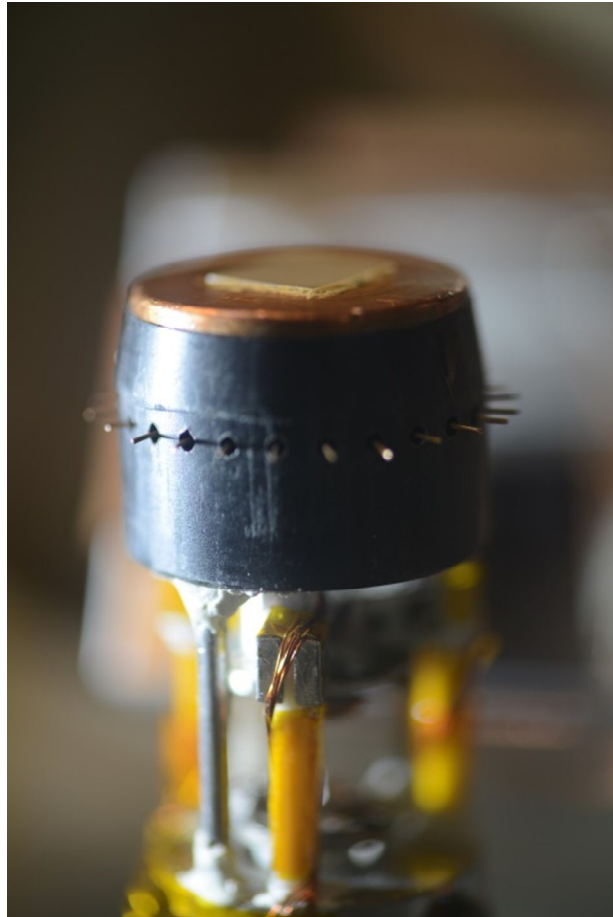


Figure 2.6.3 Photograph of the top of STM body. The leads that stick out from the Delrin piece (black material) are the electrical contacts of the STM.

We also suffered serious background noises stem from liquid nitrogen bubbling in the outer dewar. The largest spike of the current spectrum usually lies around 375Hz. We have tried two methods to eliminate this kind of noise. The first one is to moderately flow a small amount of helium gas to the bottom of the outer dewar [19]. The concept is based on Joule-Thomson effect, which

indicates the expansion of helium gas bubble can push the surrounding liquid nitrogen to nearby nitrogen bubble, the nitrogen gas does positive work during the expansion so the temperature drop (below its boiling point), and the bubbles go away. The second one is to freeze liquid nitrogen by pumping the dewar with a diaphragm pump [20]. Eventually, we adopted the second method since we found its performance be more effective, more stable, and last much longer. Typically, we pump the outer dewar for one hour, and the background noise spectrum can stay at low level (30~80 fA/Hz) for more than 6 hours.

## **Chapter 3**

### **STM scanner tube calibration**

#### **3.1 STM scanner tube calibration**

As mentioned in the previous chapter, there are many factors that can determine the quality of STM data. A well developed system plus a quiet surrounding environment are essential to acquire fine images and spectroscopy. At the earlier stage, we were only able to get the large topographical structure of the samples (Figure 3.1.1). The features within an area above  $50\text{nm}^2$  can be easily observed in raw STM data. However, we have struggled to acquire atomic resolution images thereafter for a long time.

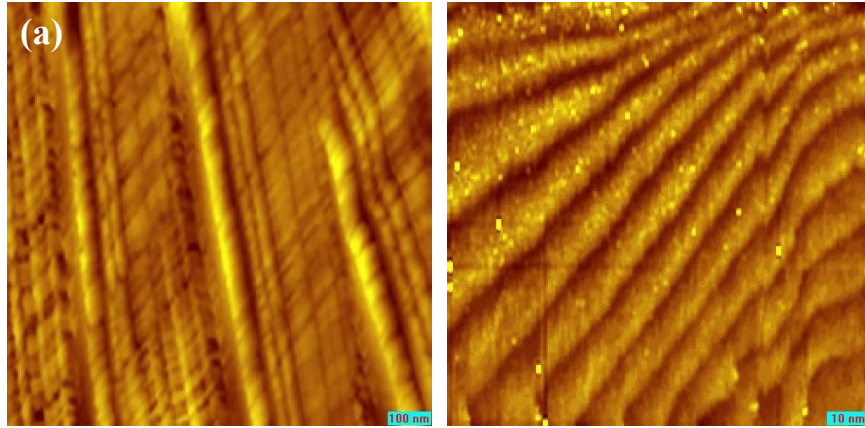


Figure 3.1.1: Large field of view of RT STM topographic images. (a) Image of  $\text{La}_{2-2x}\text{Sr}_{1+2x}\text{Mn}_2\text{O}_7$  ( $x \sim 0.32$ ), with a setpoint bias  $V = +1\text{V}$  and a setpoint current  $I = 20\text{pA}$ . The scan size is  $1 \times 1 \mu\text{m}$ . (b) Image of gold on mica, with a setpoint bias  $V = +1\text{V}$  and a setpoint current  $I = 20\text{pA}$ . The scan size is  $100 \times 100 \text{ nm}$ . The herringbone structure can be clearly observed.

We have tried numerous methods to create a good scanning condition. Well prepared tips and samples as well as a fine vibrational isolation system are prerequisites to achieve this goal. Separation of signal and high voltage wires and feedthroughs decreases the electrical noise. Removal of any possible grounding loop can reduce the 60Hz noise. The noise coming from liquid nitrogen bubbling in the outer dewar cannot be removed permanently, but we can easily decouple this noise by keeping the signal wires from touching the outer dewar.

Figure 3.1.2 shows the uncalibrated LT STM image of graphite. This image was taken under the default 80K calibrations of the R9 software, which were  $K_x$  &  $K_y = 70\text{nm/V}$  and  $K_z = -13 \text{ nm/V}$ . Although the dimension of the

structure is not correct, but we can clearly see the atomic feature of triangular pattern of HOPG. The nominal atom-to-atom distance is 0.246nm. Our observed value is about 0.75nm (Figure 3.1.2(b)), so we calibrated the lateral piezo constants to  $K_x$  &  $K_y = 22.96\text{nm/V}$ .

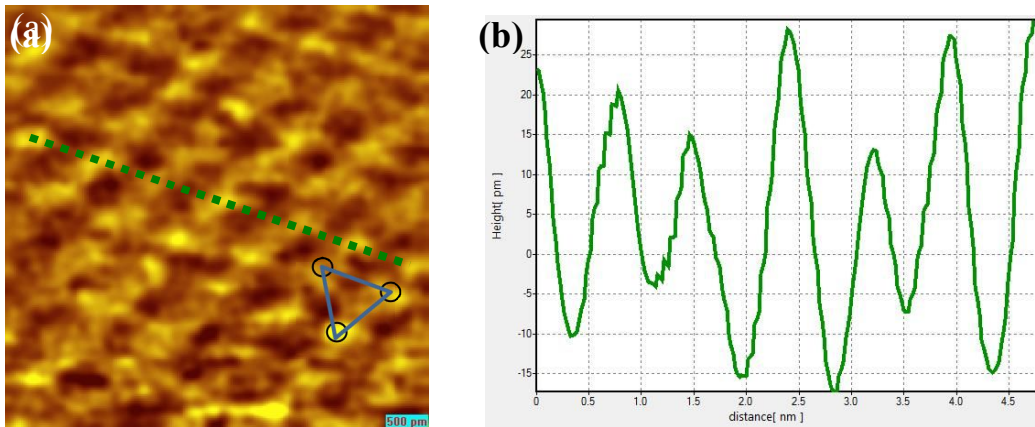


Figure 3.1.2: (a) Uncalibrated 80K STM image of HOPG. The size of image is 5x5 nm. The tunneling junction parameters were: setpoint bias  $V = +50\text{mV}$  and a setpoint current  $I = 1\text{nA}$ . The resolutions are 256 x 256 pixels, with scan speed of 62.5nm/s. (b) Contour line along the green dotted line in (a).

The dimensions of our scanner tube are one inch in length, 0.25 inch in outer diameter and 0.02 inch in thickness. According to a theoretical derivation [21], the piezo constant of PZT-5H tube at 80K should be  $K_x$  &  $K_y = 16.206\text{nm/V}$  and  $K_z = -4.5\text{nm/V}$ . Figure 3.1.3 shows the image taken under theoretical calibrations. The heights of the steps in Figure (3.1.3b) are about 0.281nm (left)

and 0.534nm (right), and the nominal lattice constant for the z axis (distance between the first and the third layer of atoms) is 0.67nm. The location of the image happened to be across four descending layers of graphite atoms, so we can roughly calibrate the vertical piezo constant to  $K_z = -5.646 \text{ nm/V}$ .

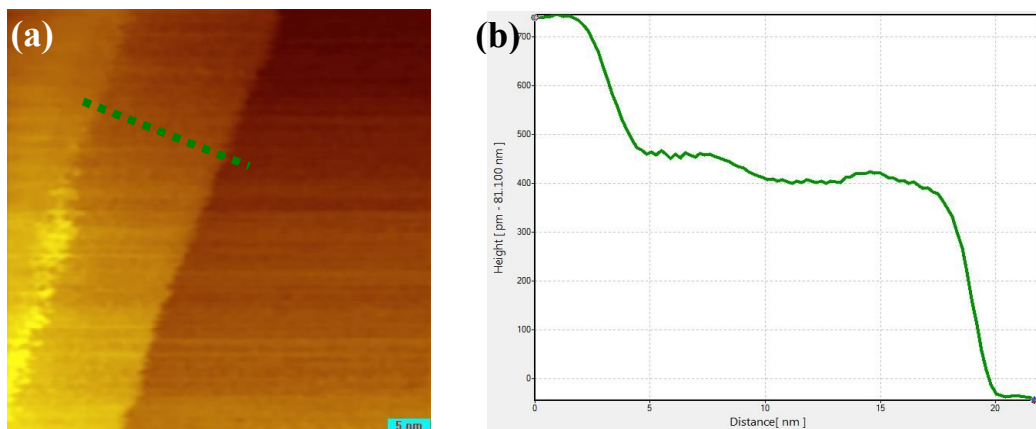


Figure 3.1.3: (a) Theoretical calibrated 80K STM image of HOPG. The size of image is 50x50 nm. The tunneling junction parameters were: setpoint bias  $V = +350\text{mV}$  and a setpoint current  $I = 1\text{nA}$ . The resolutions are 256 x 256 pixels, with scan speed of 50nm/s. (b) Contour line along the green dotted line in (a)

## Chapter 4

### STM of Cobalt clusters on HOPG

#### 4.1 Motivation

The use of spin rather than charge as the state variable in spintronic devices has been discussed widely for the past few years[22~26]. Graphene has been a popular candidate because of its high electron mobility and tunable electron filling [27]. Different kinds of spin storage cell such as dilute quantum dots [28], magnetic impurities [29], lithographic dent for magnetic materials [30] have been adopted to explore the mechanism and properties of spin-polarized conduction electrons. Spin-polarized STM is probably the most powerful tool to investigate magnetic structure at the atomic level. Yet, there is still no obvious attempt of sp-STM/STS measurement on graphene magnetic behavior so far, even though the theoretical baseline has long been predicted and constructed. To clarify the experimental feasibility of this topic, knowing the corresponding mechanism at a larger scale (down to sub-atomic level) might be a good start. In the following sections, we will explore the surface information of cobalt clusters on HOPG substrate with non-magnetic tungsten tips with focus on the difficulties one might confront in order to extract nice data.

## 4.2 The model of graphene and graphite

The carbon atoms are arranged in a honeycomb structure as shown in figure 4.2.1. The unit lattice vector  $a_1$  and  $a_2$  can be expressed as:

$$a_1 = a_0 \left( \frac{3}{2}, \frac{\sqrt{3}}{2} \right) \quad ; \quad a_2 = a_0 \left( \frac{3}{2}, \frac{-\sqrt{3}}{2} \right) \quad (4.2.1)$$

$a_0$  is the atom-to-atom distance, which is equal to 1.42Å. (Note that in figure 3.1.2, the observed triangular pattern of graphite is stemmed from a half of the unit cell which span by  $a_1$  and  $a_2$  in figure 4.2.1. Each blue sphere has a neighboring atom along c-axis in the next layer while green sphere does not. STM usually can only resolve the same category of spheres at a specific bias polarity [49]. The triangular structure usually observed in graphite is constructed by blue spheres since the adopted positive bias voltage only see the sites that have large LDOS away from Fermi surface). Its first Brillion zone is also a hexagon, with unit vectors:

$$b_1 = \frac{1}{a_0} \left( \frac{2\pi}{3}, \frac{2\pi}{\sqrt{3}} \right) \quad ; \quad b_2 = \frac{1}{a_0} \left( \frac{2\pi}{3}, \frac{-2\pi}{\sqrt{3}} \right) \quad (4.2.2)$$

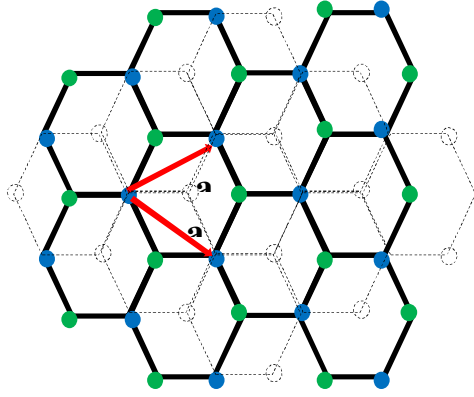


Figure 4.2.1 Atomic structure of graphene (only solid layer) and graphite (including dashed layer structure)

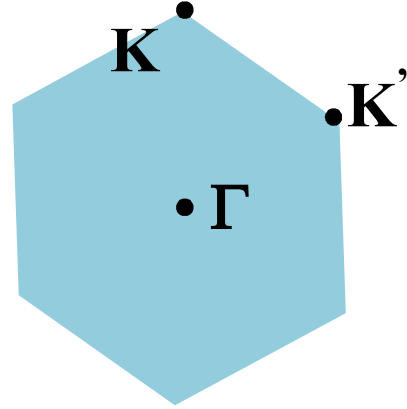


Figure 4.2.2 The first Brillion zone of graphene reciprocal lattice.

With conventional notation for points of special symmetry, three distinct symmetric points,  $K$ ,  $K'$ ,  $\Gamma$ (origin) are shown in figure 4.2.2. For most transport experiment, the low energy regime dominate, so the band structure of graphene is eligible to be derived only from the out of plane  $2p_z$  orbitals contribution, and the simplest description would be a tight-binding approximation of the hopping  $\pi_z$  electrons between nearest neighbor sites of a honeycomb lattice. The general Hamiltonian of the itinerant electrons interacting with randomly located magnetic impurities can be expressed as [46]:

$$H = -t \sum_{\langle i,j \rangle, \sigma} (c_{i,\sigma}^\dagger c_{j,\sigma} + \text{H.c.}) - 2J \sum_j s\mathbf{I} \cdot \mathbf{S}\mathbf{I} \quad (4.2.3)$$

where  $S_i$  represents the on-site magnetic moment,  $s_i$  is the spin of electrons, and  $c_{i,\sigma}^+$  creates an electron with spin  $\sigma$ ,  $\langle i, j \rangle$  are NN sites in the honeycomb lattice.

To simplify the calculation, we neglect the magnetic interaction between electrons and impurities ( $J=0$ ), and the eigenvalues of the resulting diagonalized Hamiltonian are:

$$E(k) = \pm \gamma_0 \sqrt{1 + 4 \cos\left(k_x \frac{3}{2} a_0\right) \cos\left(k_y \frac{\sqrt{3}}{2} a_0\right) + 4 \cos^2\left(k_y \frac{\sqrt{3}}{2} a_0\right)} \quad (4.2.4)$$

where  $\gamma_0$  is the nearest neighbor hopping term. Figure 4.2.3 shows

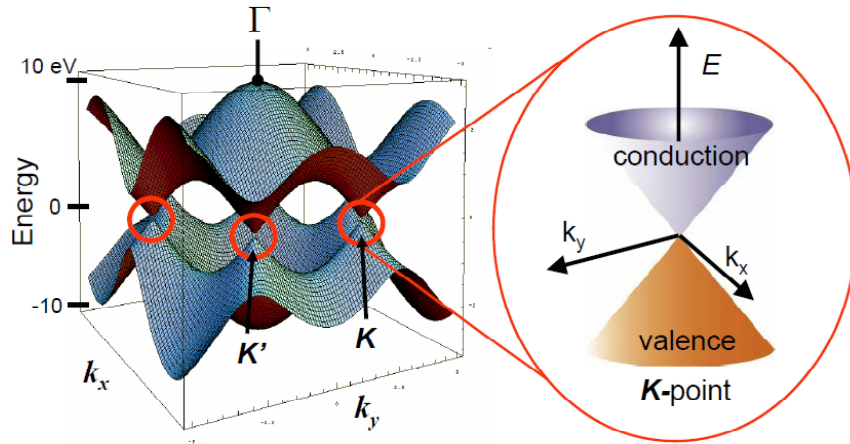


Figure 4.2.3 Simplified  $\pi$  bands of graphene[47]

the  $\pi$  bands of graphene from simplified tight-binding model in 3D dimension. The distinct feature of the figure is that the Fermi surface locate at the level of K and K' (Dirac points), where the valence and conduction bands meet. The location of the Fermi surface change (relative to the Dirac point) in accordance with the change of graphene surface charge density:

$$\Delta E = \hbar v_f \pi \sqrt{n} \quad (4.2.5)$$

where  $v_f$  is the Fermi velocity of graphene. Therefore graphene has a linear density of states characteristics that increase away from the Dirac point:

$$DOS(E) = \frac{\partial n}{\partial E} = 2E / \hbar^2 v_f^2 \pi^2 \quad (4.2.6)$$

The above equation infers that the impurities can create hole doped or electron doped sub-lattice, as the Dirac point can be moved below or above the Fermi level.

### **4.3 Electronic contribution elimination to the overall spectroscopy**

When we conduct an STM measurement, the type of sample determines what range of the tunneling parameters we are going to adopt. Our SP-STM measurement is now limited to large scale ( $>10\text{nm}^2$ ) due to magnetic material availability on our tip. A separation of spin-averaged and spin-resolved contribution to the tunneling signal can be easily fulfilled if we luckily have an electronically homogeneous sample within the observing regime. To test that, we ran traditional STM first (with non-magnetic, tungsten tip) and find an area that has clear topographic features of Co clusters. Then, we conducted  $32 \times 32$  grid I-V spectroscopy on that area. We found that it is hard to distinguish the conductivities of bare HOPG surface and cobalt clusters (Figure 4.3(b)). Therefore, we claim that in the scale of few tens/hundreds of nanometers, the magnetic properties of Co cluster on HOPG can be extracted directly from SP-STM/STS measurement with a magnetic tip. We only need to optimize the bias voltage that can generate the greatest spin asymmetry. But this result can only guarantee the current scanning area is favorable for simplified sp-STM/STS analysis. In most cases, the tunneling condition change significantly at different location, and the localized impurities can also make its electronic properties different from the bare graphite. We will furtherly discuss this topic in the following sections.

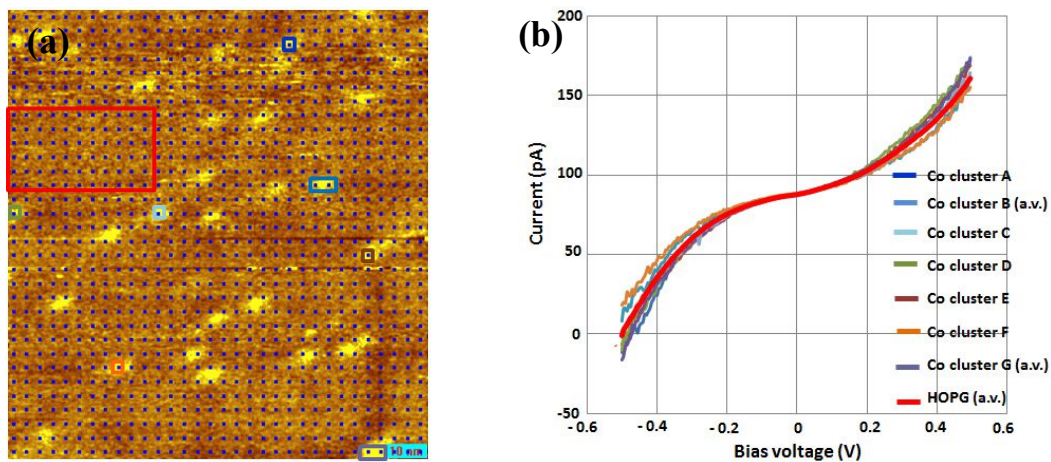


Figure 4.3 (a) STM image of Co cluster on HOPG at 80K. Size of the image is 100x100 nm. (b) I-V spectroscopic curves taken at the selected locations in (a). The curve of HOPG substrate is the averaged result of the 66 grid points in the largest box. The cobalt clusters' curves are obtained from either single points or averaged result in the colored boxes. The current axis is shifted due to an offset in the current to voltage amplifier. All curves should go through zero current at zero voltage.

#### 4.4 Identification of Cobalt clusters behavior on HOPG

The following data were obtained at the pressure level near UHV condition, with base pressure  $\sim 1 \times 10^{-9}$  torr, and the pressure inside the cryogenic garage will be at least one order of magnitude lower than that. The temperature

of the STM was 77 kelvin. With drift correction function provided by R9 software, the intrinsic thermal drift effect can be maintained at a low level. In order to verify that there are negligible adsorbed atoms on the surface after a prolonged time, we have run the experiments for over two months without changing the sample. From figure 4.4.1, we can see that randomly distributed bright spots are ubiquitous and their density did not change much after a 1.5month period. So we can rule out the possibility that the bright regions represent surface adsorbed atoms, but the deposited cobalt clusters instead.

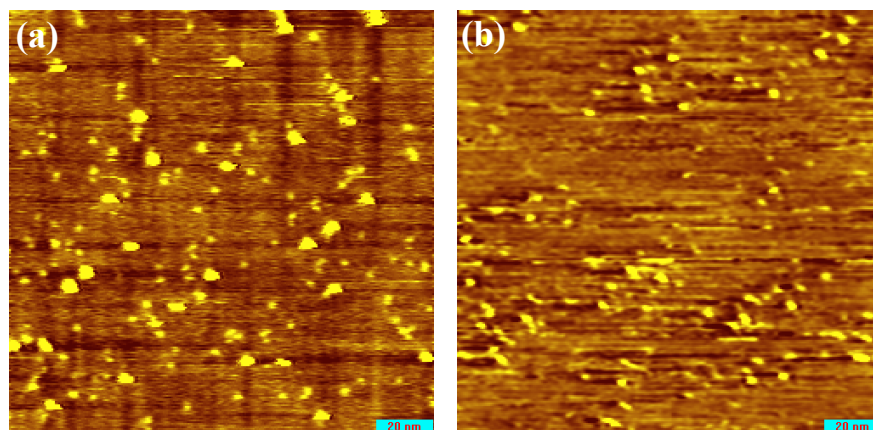


Figure 4.4.1: STM topographic images taken on (a) 5/9/2015 (b) 6/23/2015. The images have same size: 150x150nm. The tunneling parameters: setpoint bias  $V=+300\text{mV}$  and a setpoint current  $I = 800\text{pA}$ . They were acquired at different locations.

One possible obstacle of utilizing sp-STM to study graphene's magnetic properties is the highly dynamic behavior of the deposited magnetic material. Figure 4.4.2 is the STM topography of Co clusters on HOPG and its conductance

map. The image set was acquired not long after the scanning condition was stabilized. The distinct topographic feature is the protrusions with different sizes and bump heights. We consider all of them belong to same category of corrugation by looking at the conductance map.

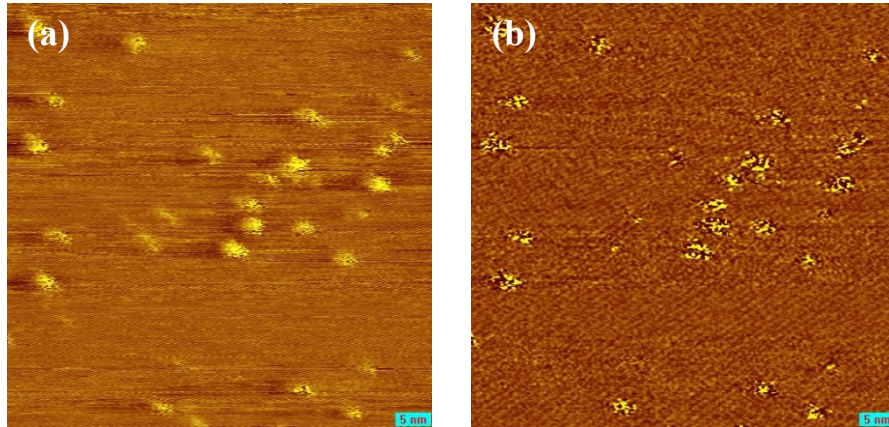


Figure 4.4.2: (a) STM topographic image of Co clusters on HOPG (b)  $dI/dV$  map of (a). The size of images is  $60 \times 60$  nm. The tunneling parameters: setpoint bias  $V = +300$  mV and a setpoint current  $I = 500$  pA.

However, if we keep scanning a localized area for hours, the surface condition might change. Figure 4.4.3 is the STM images after scanning that area for more than 12 hours. Depressions, which were not observed at the beginning, have developed. The origin of the stronger corrugation after time evolution still needs to be carefully identified. This could be caused by clusters/impurities mobility due to thermodynamics, or merely the tip function was changed (s state

changed to  $p_z$  or  $d_z^2$  state). If we refer to figure 4.4.4(B), the depth of the depression is in atomic scale.

The interesting features of this image set include: (1) The bright spots marked with green circles tend to fade off at some moment and reappear at another. (2) Depressions are persistent, but hard to distinguish spectroscopically from the bright spots (blue circles). (3) The conductance map did not show spectroscopic contrast on top of some of the clusters that are seen on the topography (orange, red, and purple circles). Note that the purple circle spot even possess significant topographic elevation. (4) The size and the relative distance of topographic features did not

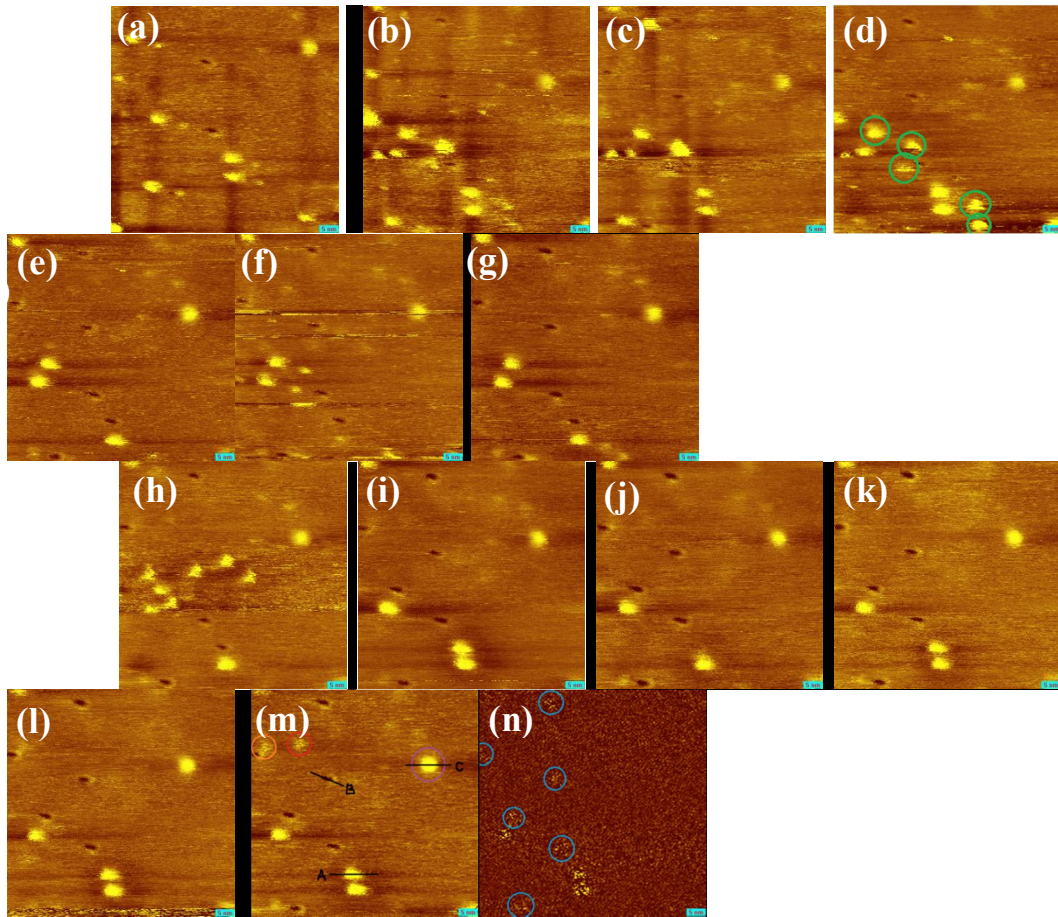


Figure 4.4.3: Consecutive STM topographic images with totally 6.5 hours acquisition time. The images have same size: 60x60nm. The tunneling parameters: setpoint bias  $V = +300\text{mV}$  and a setpoint current  $I = 500\text{pA}$ . (n) is the conductance map of (m).

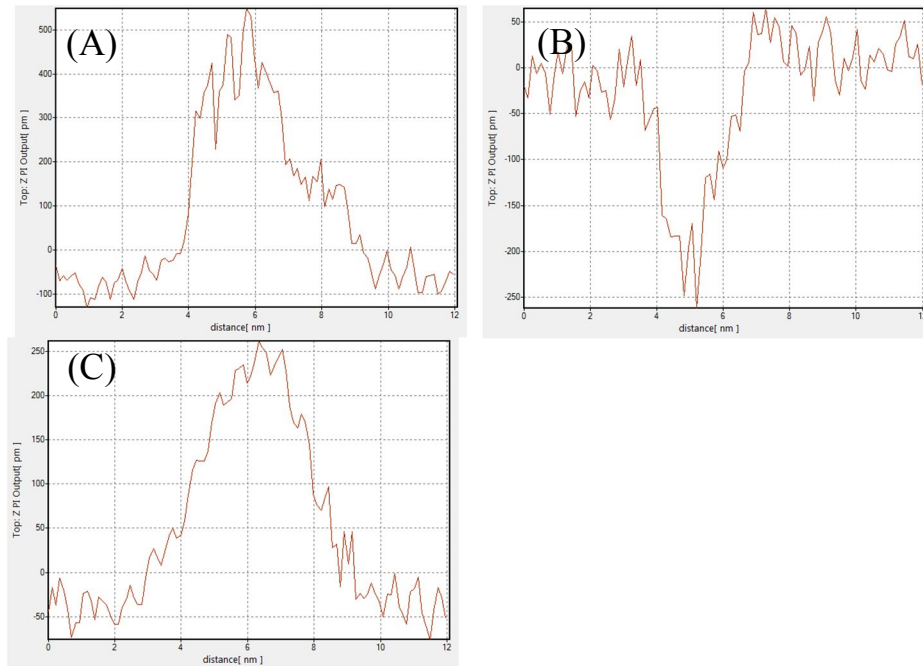


Figure 4.4.4: Contours along lines (A), (B), (C) in figure 4.4.3 (m).

change, so we can claim that there is no involved aggregation and collision mechanism between these features.

Figure 4.4.5 is the Fourier transform of the  $dI/dV$  maps in Figure 4.4.3. The modulation peak with two different wavelengths can be clearly seen. But it is hard to identify the source of modulation from the corresponding topographic images. The involved physics need to be further characterized.

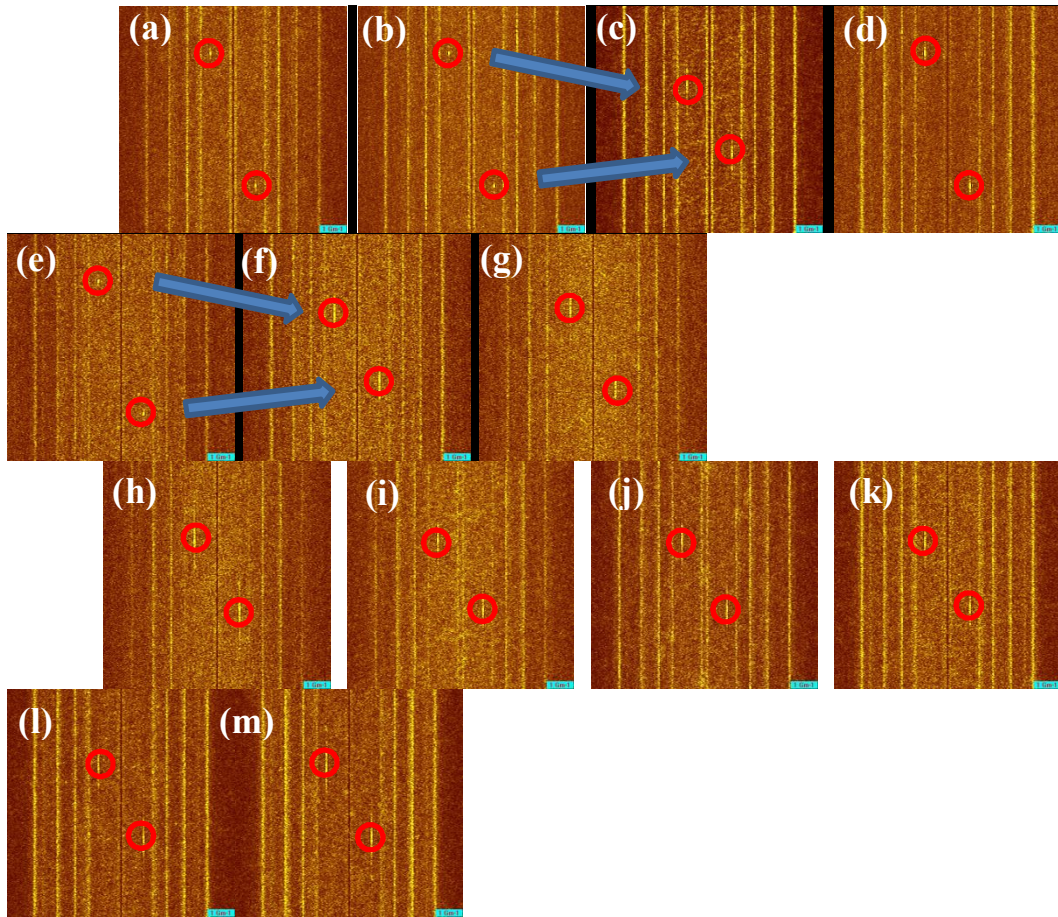


Figure 4.4.5 : 2D FFT of figure 4.4.3.

Another obstacle of utilizing sp-STM to study graphene's magnetic properties is the effectivity of spectroscopic acquirement. This challenge can also apply to nanometer-scale situation. For example, if we want to investigate the density of states at specific locations, normally we will run the topography and "simultaneous" dI/dV curve at the spots. But the bias modulation sweep can act as a minor voltage pulse, which may cause damage to the structure underneath. Refer to figure 4.4.6, we first took the image of (a), and then chose the red dots as the dI/dV curve locations(blue dots) in the next simultaneous topographic image(b). The operation of spectroscopic curve turned out to deform or erase the sample's structure, making localized analysis more difficult as a result. The possible solution would be to take the image and STS curves separately, and keep tracking the topographic images between each STS measurement to compensate lateral thermal drift. This is probably the most rigorous way for taking spectroscopy at very localized feature spots. Yet this method is time consuming, and predicting the thermal drift direction sometimes depends on luck.

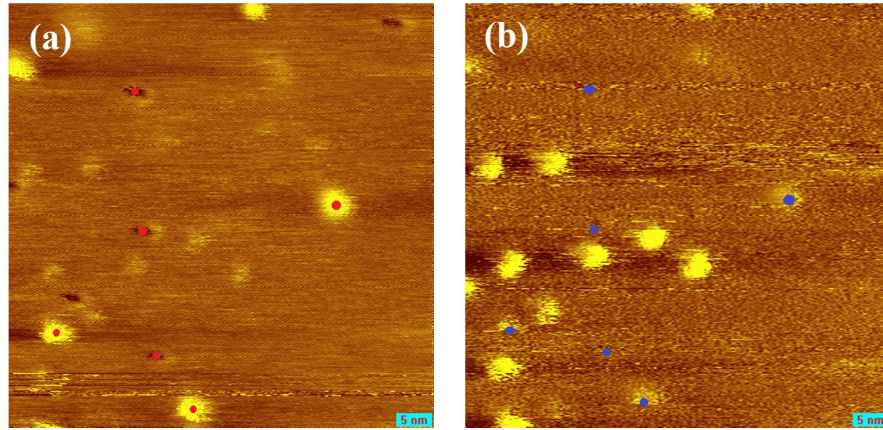


Figure 4.4.6 : Consecutive STM images. Image (b) has combined simultaneous  $dI/dV$  curves at the blue spots. The geographic distortion phenomenon at the blue spots is persistent over a wide setpoint current range.

#### **4.5 Preliminary spectroscopic study of cobalt cluster and impurities on HOPG**

As mentioned in the previous section, it is not easy to keep tracking selected localized features spectroscopically without changing their topographic structure. It is necessary to consider the intrinsic features are positioned randomly throughout the observed area. We performed simultaneous grid  $dI/dV$  curves on that area and extracted spectroscopic information from those points that have intact topographic features. As shown in figure 4.5.1(b), we picked up the curves at colored dots for sample analysis. Figure 4.5.2 is the conductance curves acquired above the Co clusters (green dots in figure 4.5.1(b)). We found a gap-

like feature central to the Fermi level, indicating the presence of Co cluster turned the graphite intrinsic properties from semimetal to insulator, which is not consistent with the I-V spectroscopic results in section 4.3. The possible explanation is the size-dependent effect. The clusters which

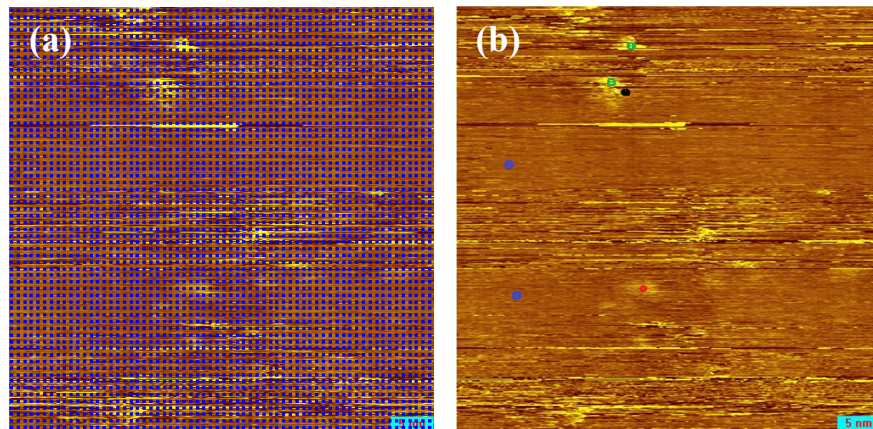


Figure 4.5.1: STM topography and simultaneous 64x64 grid dI/dV spectroscopy of Cobalt cluster on HOPG. The images have same size: 50x50nm. The tunneling parameters: setpoint bias  $V = +300\text{mV}$  and a setpoint current  $I = 100\text{pA}$ .

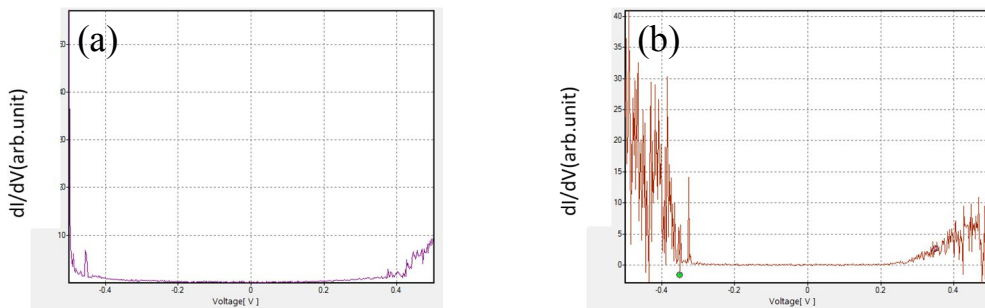


Figure 4.5.2: dI/dV curves acquired above the cobalt clusters on graphite.

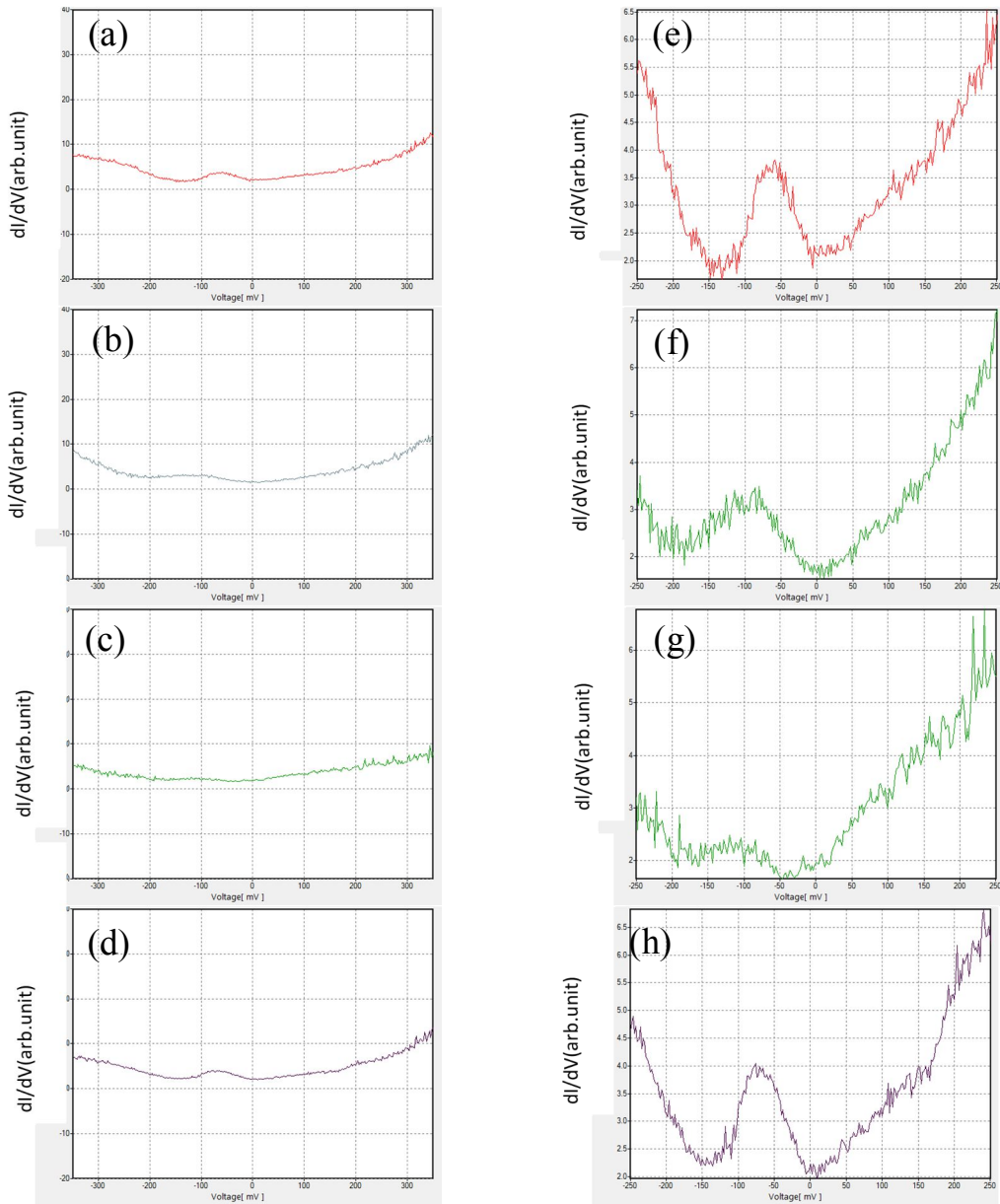


Figure 4.5.3:  $dI/dV$  curves acquired above (a,b) bare HOPG, (c) 2nm away from Co cluster and (d) localized topographic defect. Right figure set is the blow up around Fermi level of the left set.

generate the curves in figure 4.3(b) have universal protrusion height  $<1.5\text{\AA}$ , while the two clusters in figure 4.5.1 have protrusion height in the range of  $3 \sim 5\text{\AA}$ . Note that the conductivities of graphite comes from the “in plane“ motion of the free electron on the  $2p_z$  orbital which form  $\pi$  band of graphite. The physics behind this discrepancy is still unknown. We will request theoretical explanation on the contributing subtle cluster size effect.

Figure 4.5.3 are the  $dI/dV$  tunneling spectrums acquired at: (a,b) bare graphite, blue dots in figure 4.5.1(b); (c) 2nm away from the cobalt cluster, black dot in figure 4.5.1(b); and (d) localized topographic defect, red dot in figure 4.5.1(b). If we refer to the blow up of these curves, the spectroscopic trace of one of the bare HOPG match even closer to the defect than to the other bare HOPF site, indicating the electronic property of few tens of picometers height is not resolved by STS.

The shift of Dirac points (local STS minimum in the blow up figures), and the peaks around  $-70\text{meV}$  can be realized as general impurity picture. The Dirac points lie on the left hand side of the Fermi level, indicating the impurities (include clusters and defects) become ionized, and serve as an electron-doped source to the graphite surface. The source of the dominate peak at around  $-70\text{meV}$  is unknown, however, this peak was reported in the previous STS measurement on graphene [44]. The possible explanation of this peak is the hybrid vibrational electronic states, which relate to the fluctuation due to the screening of a Coulomb impurity on graphene [48, 58]. The impurities, which include the adatoms and defects on the graphene surface, can become ionized when we applied a potential difference between tip and sample [56, 57]. The

adatoms and defects on the graphene surface therefore become dopants that can be turned on and off. The similar behavior in graphite again needs to be further investigated. But as mentioned previously, we need to carefully identify if the ionization of the impurities in graphene/graphite system is their intrinsic property, or the transient phenomena caused by STS probing.

We would also like to know how the presence of Co clusters affects the electronic state of the nearby area of graphite substrate. Figure 4.5.3 (c,g) show the  $dI/dV$  spectrum 2nm away from the center of one Co cluster. The interesting feature in (g) is the 50meV shift of the Fermi level. The dominate feature is the electron pocket 50 meV below the fermi energy. It was reported in a previous STS measurement, shows that the zigzag edges can induce a peak in the local density of states at  $-30$  meV [50]. Our result matches closer to the ARPES measurement [51], which indicates: from the dispersion near K point of graphite Brillouin Zone, shows that the defect-induced localized states is a possible explanation for this large electron pocket. In fact, it has been shown that a low concentration of defects can induce self-doping to the sample [52,53]. Therefore it is worth to investigate further the properties of the electron pocket, and shed some light on the magnetic properties of graphene/graphite system, since it has been proposed that some defect-induced localized states are magnetic [54, 55].

## **4.6 Conclusions**

Reasonable STM data extraction is sometimes very demanding. Our result infers the experimental difficulties of acquiring electronic/magnetic properties of cobalt cluster on graphite, not to mention the more complicated data analysis of spin-polarized STM on graphene magnetic structure at the atomic-level. Moreover, the current literature has not yet reached a consensus of what proper tunneling  $dI/dV$  spectra of a graphene or graphite surface should look like [31-42], since the novel surface structures are position-dependent. The complex surface condition causes difficulties to engineer uniform structural defects at a large scale in HOPG or graphene which generate desirable ferromagnetism. Our goal is to provide a scenario of sound STM data acquirement, knowing the physics of manufactured graphite/graphene system, and the result would hopefully shed some lights on future sp-STM/STS analysis.

## **4.7 Suggestions for future work**

Our home-made sp-STM system has been designed and built from ground up since 2010. During time evolution, many parts have been modified, such as manipulators, electrical contact engagement of STM body, etc. The instrument's performance is satisfactory and has been taken preliminary characterization test of many kinds of samples. But if we want it to be qualified for more serious experiments in the future, there are still plenty of things to do. We will replace both liquid helium and (larger inner diameter) liquid nitrogen dewars in order to

make loading easier and superconducting magnet detachable from the inner dewar, In the means time, find the lead that is short to ground when we take out the superconducting magnet. Moreover, if we expect to conduct temperature-varied experiment under magnetic field, we have to add two heaters to the STM body, and replace the silicon diode sensor with a Cernox thermometer. Five unused electrical contacts have been reserved for this purpose, so we don't need to modify the STM head.

Another concern of acquiring good data is the reliability of tip and sample. Since the preparing methods (as mentioned in the previous sections) of the raw tungsten tip have produced nice images and spectroscopies, any fancier tip quality examinations, SEM & TEM for example, are not necessary. However, if we wish to explore the magnetic structure of deposited graphene, we do need a portable load-lock chamber to transfer the graphene. Our HOPG sample are coming from commercial supplier, and the ordinary mechanical exfoliation method [43] in air can only create very localized area that reach atomically flat standard. Searching this small area for good scanning could be time consuming, so we will run a dehumidifier in the room at all time for the experiment.

The defect on graphite, as well as oxygen contamination or residual gases even under UHV environment, can cause significant influence on the electronic and magnetic properties of cobalt clusters. Besides sp-STM/STS, other techniques such as Angle-resolved photoemission spectroscopy (ARPES) might also be combined to the research for comparative structural analysis.

## Appendix

### Program Code

```
[START]
out 888.255
for j=1 to 68000 : next
out 888.0
for j=1 to 68000 : next
go to [START]
```

## Bibliography

- [1] C. J .Chen, 1993 *Introduction to Scanning Tunneling Microscopy* (New York : Oxford University Press)
  
- [2] C. J .Chen, *Phys. Rev. B*, **42**, 8841-8857 (1990a).
  
- [3] D. Wortmann, S. Heinze, P. Kurz, G. Bihlmayer, and S. Blugel, *Phys Rev Lett.* **86**, 18, 4132-4135 (2001).
  
- [4] M. Bode, M. Getzlaff M and R. Wiesendanger, *J. Vac. Sci. Technol. A* **17** 2228 (1999a).
  
- [5] R. Wiesendanger, *Review of Modern Physics* **81**, October-December (2009).
  
- [6] S. H. Pan, International Patent WO93/19494 (30 September 1993); The design is also described in S. H. Pan, E. W. Hudson, and J. C. Davis, *Rev.Sci. Instrum.* **70**, 1459 (1999).
  
- [7] T.-M. Chuang and A. de Lozanne, *Rev. Sci. Instrum.* **78**, 053710 (2007).
  
- [8] S. Kweon, N. Samarth, and A. de Lozanne, *J. Appl. Phys.* **105**, 093906 (2009).
  
- [9] S. H. Kim, and A. de Lozanne, *Rev.Sci. Instrum.* **83**, 103701 (2012).
  
- [10] G. Binnig and D. P. E. Smith, *Rev. Sci. Instrum.* **57**, 1688 (1986).
  
- [11] D. W. Pohl, *Rev. Sci. Instrum.* **58**, 54 (1987).

- [12] J. W. Lyding, S. Skala, J. S. Hubacek, R. Brockenbrough, and G. Gammie, *Rev. Sci. Instrum.* **59**, 1897 (1988).
- [13] See *Appendix I* for Liberty BASIC.
- [14] L.J. Chen, S. H. Kim, A. K. Lee, and A. de Lozanne, *Rev. Sci. Instrum.* **83**, 013708 (2012).
- [15] J. P. Ibe, P. P. Bey, S. L. Brandow, and R. A. Brizzolara, *J. Vac. Sci. Technol. A* **8**, 3570 (1990).
- [16] T. Fleisch, A. T. Shepard, T. Y. Ridley, W. E. Vaughn, N. Winograd, W. E. Baitinger, G. L. Ott, and W. N. Delgass, *J. Vac. Sci. Technol.* **15**, 1756 (1978).
- [17] Barry Controls, model SLM 12A.
- [18] S. H. Kim and A. de Lozanne, *J. Vac. Sci. Technol.* **31**, 013201 (2013).
- [19] Larry Kevan. "Prevention of liquid nitrogen bubbling in electron spin resonance samples". *Concepts in Magnetic Resonance*. Volume 1, Issue 2, page 131, October (1989)
- [20] Umrath, W. (1974). "Cooling bath for rapid freezing in electron microscopy". *Journal of Microscopy* **101**: 103–105
- [21] C. Julian Chen. *Appl. Phys. Lett.* **60**, 1 (1992).
- [22] J. Tworzydło, B. Trauzettel, M. Titov, A. Rycerz, and C. W. J. Beenakker, *Phys. Rev. Lett.* **96**, 246802 (2006).

- [23] S. V. Morozov, K. S. Novoselov, M. I. Katsnelson, F. Schedin, L.A. Ponomarenko, D. Jiang, and A. K. Geim, *Phys. Rev. Lett.* **97**, 016801 (2006).
- [24] K. Novoselov *et al.*, *Nature*, London **438**, 197 (2005)
- [25] K. Novoselov *et al.*, *Nat. Phys.* **2**, 177 (2006).
- [26] A. H. Castro Neto *et al.*, *Rev. Mod. Phys.* **81**, 109 (2009).
- [27] I. Žutić, J. Fabian, and S. Das Sarma, *Rev. Mod. Phys.* **76**, 323 (2004).
- [28] S. Chakrabarti and A.J. Pal, *J.Phys.Chem.C*, **118**, 25786–25791 (2014)
- [29] M. Daghofer, N. Zheng, A. Moreo, *Phy. Rev B*, **82**, 121405 (2010).
- [30] Tapaszto, L.; Dobrik, G.; Lambin, P.; Biro, L. P. Tailoring the Atomic Structure of Graphene Nanoribbons by Scanning Tunnelling Microscope Lithography. *Nat. Nanotechnol.*, **3**, 397–401 (2008).
- [31] N. Agrait *et al.*, *Ultramicroscopy* **42-44**, 177 (1992); R. J. Colton *et al.*, *Journal of Vacuum Science & Technology A: Vacuum, Surfaces, and Films* **6**, 349 (1988).
- [32] S. Marchini *et al.*, *Physical Review B* **76**, 075429 (2007).
- [33] H. Kambara *et al.*, *Japanese Journal of Applied Physics*, **45**, (1909).
- [34] Y. Niimi *et al.*, *Physical Review B*, **73** (2006).

- [35] G. M. Rutter *et al.*, *Science* **317**, 219 (2007).
- [36] O. I. Shklyarevskii *et al.*, *Applied Physics A* **81**, 1533 (2005).
- [37] G. Li *et al.*, *Nat Phys* **3**, 623 (2007).
- [38] L. Vitali *et al.*, *Physical Review B* **69**, 121414 (2004).
- [39] Y. Zhang *et al.*, *Nat Phys* **4**, 627 (2008).
- [40] V. W. Brar *et al.*, *Appl. Phys. Lett.* **91**, 122102 (2007).
- [41] D. P. E. Smith *et al.*, *Appl. Phys. Lett.* **49**, 1641 (1986).
- [42] K. Nagaoka *et al.*, *Japanese Journal of Applied Physics* **45**, L469 (2006);
- [43] K. S. Novoselov *et al.*, *Science* **306**, 666 (2004).
- [44] X. H. Qiu *et al.*, *Physical Review Letters* **92**, 206102 (2004).
- [45] R. Saito *et al.*, *Physical Properties of Carbon Nanotubes* (Imperial College Press, London, 1998)
- [46] M. Daghofer *et al.*, *Physical Review B*, **82**, 121405 (2010).
- [47] Y. Zhang, in *Physics* (Columbia University, New York, 2006), p. 94.
- [48] A. V. Shytov *et al.*, *Physical Review Letters* **99**, 246802 (2007)

- [49] S. Gwo, C.K. Shih, *Physical Review B*, **47**, 13059(R) (2008).
- [50] Kobayashi, Y., Fukui, K.-I., Enoki, T., Kusakabe, K. & Kaburagi, Y., *Phys. Rev. B* **71**, 193406 (2005).
- [51] S.Y. Zhou, *Nat Phys*, **2**, 595 (2006).
- [52] Pereira, V. M., Guinea, F., Lopes Dos Santos, J. M. B., Peres, N. M. R. & Castro Neto, A. H. *Phys. Rev. Lett.* **96**, 036801 (2006).
- [53] Peres, N. M. R., Guinea, F. & Castro Neto, A. H. *Phys. Rev. B* **73**, 125411 (2006).
- [54] Nakada, K., Fujita, M., Dresselhaus, G. & Dresselhaus, M. S. *Phys. Rev. B* **54**, 017954 (1996).
- [55] Wakabayashi, K., Fujita, M., Ajiki, H. & Sigrist, M. *Phys. Rev. B* **59**, 008271 (1999).
- [56] N. A. Pradhan *et al.*, *Phys. Rev. Lett* **94**, 076801 (2005).
- [57] F. Marczinowski *et al.*, *Physical Review B* **77**, 115318 (2008).
- [58] V. M. Pereira *et al.*, *Physical Review Letters* **99**, 166802 (2007).

## **Vita**

LeuJen Chen was born in Taipei, Taiwan on September 24<sup>th</sup>, 1982. He entered National Taiwan Normal University in Taipei, 2001. After receiving the degree of Bachelor of Science from there in 2005, he worked in the 2<sup>nd</sup> air control center of R.O.C. Air Force to fulfill mandatory military service. 2007, after completing his enlistment, he worked with Prof. Ming-Che Chang in National Taiwan Normal University as research assistant for the theoretical studies of Bose Einstein Condensation. He applied to the University of Texas at Austin for the enrollment in their physics program. He was accepted and started graduate studies in August, 2008.

Permanent address: 7F, NO.448, Xizang Rd., Wanhua District  
Taipei, Taiwan

---